2023

Modeling of Transport in Anatomic Respiratory Airways: Applications in Targeted Drug Delivery and Airborne Pathogenic Transmissions

Mohammad Mehedi Hasan Akash
South Dakota State University, mohammad.akash@sdstate.edu

MODELING OF TRANSPORT IN ANATOMIC RESPIRATORY AIRWAYS: APPLICATIONS IN TARGETED DRUG DELIVERY AND AIRBORNE PATHOGENIC TRANSMISSIONS

Mohammad Mehedi Hasan Akash

A thesis submitted in partial fulfillment of the requirements for

the

Master of Science

Major in Mechanical Engineering

South Dakota State University

2023

THESIS ACCEPTANCE PAGE

Mohammad Mehedi Hasan Akash

This thesis is approved as a creditable and independent investigation by a candidate for the master's degree and is acceptable for meeting the thesis requirements for this degree. Acceptance of this does not imply that the conclusions reached by the candidate are necessarily the conclusions of the major department.

Saikat Basu
Advisor Date

Yucheng Liu
Department Head Date

Nicole Lounsbery, PhD
Director, Graduate School Date

Dedicated to my parents Selina Hossain and Mozaffor Hossain; to my wife Ayesha Tasnim; and to my younger brother Mahin Hasan Abash.

Acknowledgments

I am deeply grateful to my parents, Selina Hossain and Mozaffor Hossain, for their unwavering support and inspiration throughout my academic and personal endeavors. Without their encouragement, I would not have achieved all that I have. My wife, Ayesha Tasnim, has been an invaluable source of motivation and encouragement. Her constant belief in me has been essential in keeping me focused on my goals during this challenging journey. I would also like to express my appreciation to my younger brother, Mahin Hasan Abash.

Most importantly, I owe a debt of gratitude to my advisor, Dr. Saikat Basu, for his invaluable guidance and mentorship over the past two and a half years. Under his expert guidance, I have been fortunate enough to pursue a vital phase of my academic career. I feel blessed to have had the privilege of working with such a knowledgeable and supportive mentor. I would also like to express my gratitude to my committee members, Dr. Zhong Hu and Dr. Semhar Michael, for their invaluable support and guidance throughout my research. My lab-colleague, Abir Malakar, also deserves recognition for his assistance and support.

Finally, I would like to extend my sincere thanks to the staff members at the Department of Mechanical Engineering, specifically Adeline Flaskey, for her assistance with the administrative details that are essential to the successful completion of this project.

Contents

List of Abbreviations

CFD = Computational Fluid Dynamics

CI = Confidence Interval

COVID-19 = Coronavirus Disease 2019

CPAP = Continuous Positive Airway Pressure

CT = Computed Tomography

CU= Current Use

DICOM = Digital Imaging and Communications in Medicine

GERD = Gastroesophageal Reflux Disease

IU= Improved Use

L/min = Liters per minute

LES = Large Eddy Simulation

OR = Odds Ratio

OSA = Obstructive Sleep Apnea

PCR = Polymerase Chain Reaction

RNA = Ribonucleic Acid

RT = Reverse Transcription

SARS-CoV-2 = Severe Acute Respiratory Syndrome Coronavirus 2

STL = Stereolithography

List of Figures

List of Tables

ABSTRACT

MODELING OF TRANSPORT IN ANATOMIC RESPIRATORY AIRWAYS: APPLICATIONS IN TARGETED DRUG DELIVERY AND AIRBORNE PATHOGENIC TRANSMISSIONS

Mohammad Mehedi Hasan Akash

2023

This thesis aims to explore the potential of improving the efficacy of drugs for treatment of viral infections by targeting the nasopharynx, which is commonly the first site of infection for many viral pathogens. Currently, intranasal sprays are used, but the standard protocol ("Current Use" or CU) results in suboptimal drug deposition at the nasopharynx. To address this issue, an "Improved Use" or, IU protocol has been proposed, which involves pointing the spray bottle at a shallower angle and aiming slightly towards the cheeks. The IU delivery is also robust to perturbations in spray direction, which highlights the practical utility of this new drug administration protocol. The results of the simulation are experimentally verified using a 3D-printed airway cavity of a different subject.

Next with the smallpox virus as an example pathogen, a numerical modeling framework for airborne respiratory diseases has been made. This modeling framework shows that the regional deposition of virus-laden inhaled droplets at the initial infection site (for smallpox, this is the oropharynx and the lungs) peaks for the droplet size range (8–27 μm for oropharyngeal deposition, and $\leq$ 14 μm for lungs) and can be used to determine the number of virions required to launch the infection in a subject.

Subsequently, to explore the mechanics of lower airway disease progression, we have considered SARS-CoV-2. We have investigated the spread of SARS-CoV-2 from the nasophar-

ynx to the lower airway. Using computational models, the inhalation process has been tracked with quantification for the volume of nasopharyngeal liquid transmitted to the lower airspace during each aspiration. The results suggest that a significant amount of liquid may be aspirated each day, which could lead to an increased risk of aggressive and accelerated lung infections in individuals with conditions like dysphagia.

Finally, in view of the high cost and time required for conducting numerous numerical simulations, we have checked Machine Learning platforms as an alternative method for predicting regional deposition at various anatomical regions based on the geometric features of the anatomic flow domains in respiratory physiology.

As an ancillary topic, the thesis also explores the morphological characteristics of the nose and their influence on airflow patterns and heat transfer dynamics inside the nasal cavity of a pig's nose. The findings indicate that tortuosity has a crucial role in particle capture efficiency, particularly in high-olfactory mammalian species such as pigs and opossums. Understanding the fluid-particle interactions in nasal cavities could lead to the development of nature-inspired designs for various engineering processes, such as the creation of novel filtration devices. Therefore, it is essential to continue investigating the significance of heat management and particle screening in nasal structures to reveal their mechanistic functions and translate this information into practical applications.

List of peer-reviewed publications based on this thesis

1. Akash, M.M.H., Lao, Y., Balivada, P.A., Ato, P., Ka, N.K., Mituniewicz, A., Silfen, Z., Suman, J., Chakravarty, A. and Joseph-McCarthy, D., and Basu, S. On a model-based approach to improve intranasal spray targeting for respiratory viral infections. Frontiers in Drug Delivery, in press, 2023. Pre-peer review version at medRxiv. doi: https://doi.org/10.1101/2022.01.26.22269854.

2. Yuk, J., Akash, M.M.H., Chakraborty, A., Basu, S., Chamorro, L.P. and Jung, S. Morphology of pig nasal structure and modulation of airflow and basic thermal conditioning. Integrative and Comparative Biology, 2023. doi: https://doi.org/10.1093/icb/icad005

3. Basu, S., Akash, M.M.H., Hochberg, N.S., Senior, B.A., Joseph-McCarthy, D. and Chakravarty, A. From SARS-CoV-2 infection to COVID-19 morbidity: an in silico projection of virion flow rates to the lower airway via nasopharyngeal fluid boluses. Rhinology Online, 5(5), 2022. doi: http://doi.org/10.4193/RHINOL/21.053. media coverage: https://www.news-medical.net/news/20220204/Understanding-how-COVID-19-infection-spreads-from-the-upper-airways-to-the-lungs.aspx.

List of conference presentations related to this thesis

1. Akash, M.M.H., Silfen, Z., Joseph-McCarthy, D., Chakravarty, A. and Basu, S., 2023. Session 2: Can machine learning predict particle deposition at specific intranasal regions based on computational fluid dynamics inputs/outputs and nasal geometry measurements?. South Dakota State University Data Science Symposium, 2023.

2. Akash, M.M.H., Tummala, A. and Basu, S. When fluid mechanics meets virology: revisiting smallpox–a modeling framework for its airborne transmission. Bulletin of the American Physical Society, 2022.

3. Akash, M.M.H., Mituniewicz, A., Lao, Y., Balivada, P., Ato, P., Ka, N., Silfen, Z., Chakravarty, A., Joseph-McCarthy, D. and Basu, S. A better way to spray?-a model-based optimization of nasal spray use protocols. In APS Division of Fluid Dynamics Meeting Abstracts (pp. Q14-007), 2021.

Chapter 1

Introduction

1.1 Thesis overview

The global respiratory pandemic [5] caused by the severe acute respiratory syndrome coronavirus 2 (SARS-CoV-2) has thrust the field of fluid mechanics back into the public eye, perhaps for the first time since the precarious era of the 1960s' space race [6].

Flow physics plays an essential role in almost every aspect of respiratory infections; none the more so than in the targeted delivery of drugs to the infection hot-spots along the airway. The causative agent for coronavirus disease 2019 (COVID-19) has been linked [7, 8] to a remarkable pattern of relatively high infectivity in ciliated epithelial cells along the nasal passage lining in the upper airway, moderate infectivity in cells lining the throat and bronchia, and relatively low infectivity in lung cells. Such viral trends are governed by the abundance of angiotensin-converting enzyme 2 (ACE2), a single-pass type I membrane protein that is exploited by the viral spike protein binding as a gateway for cellular entry. ACE2 is abundant on ciliated epithelial cells but is highly expressed in only a smaller subset of the alveolar cells in the lower airway [9]. These findings [7, 8] are nonetheless for *in vitro* samples; virus-laden droplets deposited along the anterior nasal airway might not be so effective at launching an infection despite the presence of ciliated cells, as the thicker mucus layer there provides some level of protection against virus invasion and infection [6]. Hence, the *nasopharynx*, which is the region in the upper airway posterior to the septum comprising the superior portion of the pharynx, has been postulated to be a dominant initial

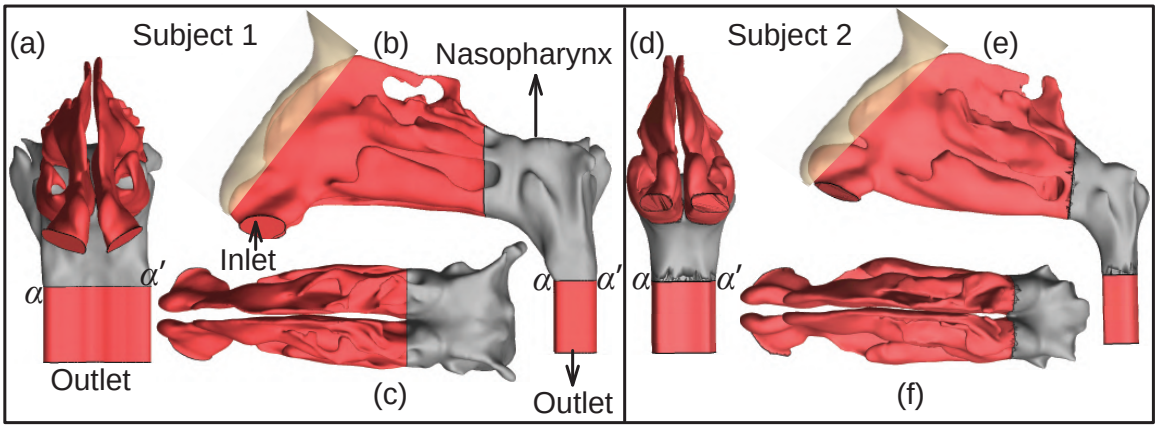

Figure 1.1: Panels (a), (b), and (c) respectively show the coronal, sagittal, and axial views of the computed tomography (CT) based upper airway reconstructions for Subject 1; panels (d), (e), and (f) show the corresponding views for Subject 2. Nasopharynx is marked in grey. Additionally, $\alpha - \alpha'$ shows the location of the wetted perimeter used while estimating the hydraulic radius.

infection site for SARS-CoV-2 [1]. Efficacy of nasopharyngeal swabs over oropharyngeal swabs for accurate detection [10] of COVID-positive cases supports the hypothesis. Based on the brisk pace at which lower airway infections ensue following the emergence of initial symptoms [7], it may be conjectured that the nasopharynx (marked in Figure 1.1, see Panels (a)-(f)) acts as the seeding zone for the subsequent spread of the disease to the lungs via lower airway aspiration of virus-laden boluses of nasopharyngeal fluids.

While this conjectured mechanism is superficially plausible, a key unanswered question is whether the rate of virion flow from the initial site of infection to the lower airway would be sufficiently high to account for a rapid onset of secondary infections at the lungs. In this thesis, we have combined earlier data on aspiration trends [11, 12] with virological assessments of sputum in COVID-positive patients [13] and our computational findings on the physical flow variables in anatomically realistic airway domains – to quantify bolus-borne virion transmission rates from the nasopharynx into the lower airway.

A continuing concern is the mutation rate of a virus and how the nature of the fitness landscape renders it amenable to evolution, potentially resulting in more virulent strains [14, 15]. A nasal spray – that can administer nasal hygiene products, antiviral prophylactics, and therapeutics – would address the concerns if it can efficiently deliver the pharmaceutics at the

virus-affected upper airway sites, thereby reducing the risk of viral droplet/aerosol shedding [16, 17] as well as mutation within the host [18, 19].

Synergizing inhaled particulate dynamics with virologic and epidemiologic data, can address questions like: (a) what are the hazardous particulate sizes predominantly responsible for infection onset, or (b) what might be the minimum number of virions (i.e., the infectious dose) that can launch an infection. These questions can be answered through experimentally-validated computational fluid dynamics (CFD) modeling of the respiratory transport process in computed tomography (CT)-based anatomically realistic upper airway geometries.

The primary objectives of this thesis are to devise an optimized approach for administering drugs through the nasal route to the affected site; to verify the efficacy of this approach through empirical experimentation; to construct a computational model capable of forecasting the hazardous droplet size and infectious dosage for respiratory diseases that spread through airborne transmission; to use machine learning as a new tool to predict regional deposition along the human respiratory airspace using geometric features of anatomies; and to investigate the thermal characteristics present within the nasal cavity and tracking particle capture trends in bio-inspired channels.

In order to reduce the operating costs of numerical simulation, we applied machine learning as a new method in this thesis to forecast regional deposition along the human pulmonary airspace utilising geometric features of anatomies. At the end of this thesis, we studied fundamental thermal transport processes in a pig's nose. We can concentrate on bridging the gap between thermo-fluid physics and biological research. Animals are constantly exchanging heat and mass with their surroundings, allowing them to adapt to a variety of environmental situations. Animal evolution has made it possible to adapt to constantly changing environmental conditions effectively [20]. The constant exchange of heat and mass with their surroundings is a key component of that process. The nose is one of the most distinctive features of animals; it efficiently carries and thermally pre-conditions the

outside air before it enters the body. The air that is inhaled quickly becomes warmed and humidified in the nasal canal when it comes into touch with the mucosa. According to research, before the inspired air reaches the pharynx, it is warmed to 35°C from 23°C outside and regulated with 98% relative humidity. This is essential for maintaining/protecting the lungs' interior, delicate structures [21, 22, 23]. The Weddell seal, the world's southernmost animal, is a striking example. Its nasal cavity contains labyrinthine structures that help it warm the air it breaths, which is between -3°C and -26°C [24, 25].

To summarize, the rest of the thesis has been organized into the following segments:

- Section 1.2 of the current chapter 1 outlines the creation of a 3D anatomy model generated from a CT scan of the human anatomy, as well as the numerical simulation modeling techniques employed

- Chapter 2 focuses on the modeling of intranasal drug delivery, with a particular emphasis on the "Improved Use" method for enhancing drug efficacy at infectious sites.

- Chapter 3 details the experimental validation of the numerical modeling approach.

- Chapter 4 presents the numerical modeling of airborne respiratory infections, which is extended to lower airway onset.

- Chapter 5 represents machine learning as a cost-effective approach to predict regional deposition along the human respiratory airspace using anatomical geometric features.

- Chapter 6 explores the thermal transport process within the nasal cavity of pigs and tracking particle capture trends in bio-inspired channels.

- Chapter 7 summarizes the limitations, comprehensive impacts, and ramifications expected from this thesis work.

1.2 Modeling principles

To access and use CT scan data, the necessary authority must be present. This can entail getting consent from the patient and any applicable regulatory organisations. The Institutional Review Board (IRB) of the University of North Carolina (UNC) at Chapel Hill granted exempt status to our thesis, allowing us to use the archived and anonymised medical records without obtaining informed consent in order to conduct retrospective computational research. In order to create a 3D model of the desired anatomy, the CT scan data must be processed using software like MIMICS. For all of our studies, we used Mimics Research v18.0 in our thesis (Materialise, Plymouth, Michigan). This can involve segmentation, smoothing, and other processing procedures to provide a thorough and accurate picture of the anatomy. After the 3D model has been created, it must be meshed so that it may be put to use in a numerical simulation. ICEM software is often used to create a prism mesh for this. We employed ICEM-CFD 2019 R3 in our research (ANSYS Inc., Canonsburg, Pennsylvania). Prism meshing is crucial in the case of a 3D anatomy created from CT scan data. The anatomy's intricate geometry can make it challenging to produce a high-quality mesh that faithfully captures the flow behaviour. Even for complex geometries with numerous small features, prism meshing may produce a mesh with a high degree of precision and stability. A typical mesh for a 3D anatomy created from CT scan data, for instance, might have between 4 million and 7 million elements, with a lot of prisms close to the surface of the anatomy to capture boundary layer effects. The input for numerical simulation tools like finite volume solvers would then be this mesh. After the mesh has been created, the numerical simulation in the solver needs to be set up. The flow conditions, boundary conditions, and other variables that are pertinent to the situation being simulated must be defined in this process. Iterating through the mesh and solving the fluid equations at each node or element using a combination of linear and nonlinear solvers is the common solution procedure. ANSYS 2019 R3 was employed in our research. The simulations were all

executed using 3.1 GHz, 4-processor, parallel computations on Xeon nodes.

The next piece in this puzzle involves the breathing parameters. Allometric relations [26] for breathing parameters are,

For males (while sitting awake),

$$\dot{Q} = (1.36 \pm 0.10)m^{0.44\pm0.02} \tag{1.1}$$

For females (while sitting awake),

$$\dot{Q} = (1.89 \pm 0.40)m^{0.32\pm0.06} \tag{1.2}$$

Here $\dot{Q}$ is the minute volume in liters per minute, and m is the body mass in kilograms. In general, inspiratory rates can stretch over 15 to 85 L/min, based on whether the individual is inhaling gently or breathing in forcefully. In my study, I have used computational fluid dynamics (CFD) in anatomically realistic upper airway geometries to simulate droplet transmission at four different inhalation rates, viz. 15, 30, 55, and 85 Liters/min [27].

Chapter 2

Numerical modeling of intranasal drug delivery

2.1 Overview

The primary site for viral infection in the upper respiratory tract is the nasopharynx located at the back of the nose. However, the standard protocol ("Current Use", or CU) for using intranasal sprays requires the nozzle to enter the nose almost vertically, resulting in less-than-optimal drug deposition in the nasopharynx. In this study, We used the Large Eddy Simulation technique to replicate the airflow in anatomically accurate human airway cavities, with varying inhalation rates and different spray axis placements and orientations. The study revealed an "Improved Use" (or, IU) spray usage protocol, where the spray bottle is aimed at a shallower angle, almost horizontally at the nostril, and slightly toward the cheeks.

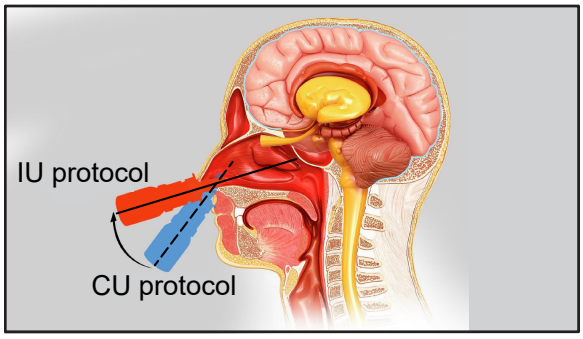

Figure 2.1: The schematic shows the two tested nasal spray usage protocols, *viz.* "Current Use" (or CU, represented by the dashed line) and "Improved Use" (or IU, represented by the solid line). Cartoon illustration is by the Dr. Ferrer Biopharma (Hallandale Beach, FL) graphics design team.

The related simulations replicate sprayed drug transmission against two different ambient inhalation rates, *viz.* 15 and 30 L/min; standing in respectively for steady relaxed and moderately heavy breathing conditions [26]. While the nasal sprays do provide a simple, yet

robust, drug delivery modality, especially during the infection onset phase of respiratory viruses; with the choice comes at least two key open questions, *viz*. (a) what are the intranasally sprayed drug droplet sizes that would maximize targeted delivery at the initial dominant infection site, the nasopharynx? and (b) is there a way to revise the nasal spray usage protocols with prevalent spray products, to enhance the delivery of targeted drugs at the infected site? This study addresses the above questions through computational fluid dynamics (CFD) modeling of the respiratory transport process in computed tomography (CT)-based anatomically realistic upper airway geometries.

Both Chapter 2 and upcoming Chapter 3 are adapted from our peer-reviewed and accepted manuscript, in press at Frontiers in Drug Delivery (2023) under the title "On a model-based approach to improve intranasal spray targeting for respiratory viral infection".

2.2 Materials and Methods

2.2.1 Anatomic upper airway reconstruction

The *in silico* upper airway geometries used in this study were digitally reconstructed from de-identified medical-grade CT imaging data derived from two healthy test subjects. Subject 1 was a 61 year-old male and Subject 2 was a 37 year-old female. For subsequent experimental validation of the *in silico* findings, we have also used a 3D-printed solid anatomic replica of a 41 year-old male subject's nasal cavity. The use of the archived and anonymized medical records was approved with exempt status by the Institutional Review Board (IRB) of the University of North Carolina (UNC) at Chapel Hill, with the requirement of informed consent waived for retrospective use in computational research.

In terms of imaging resolution, the CT slices of the airway cavities were extracted at coronal depth increments of 0.348 mm in Subject 1's scans and 0.391 mm in Subject 2's scans. Digitization of the anatomic airspaces was carried out on the image processing software Mim-

ics Research v18.0 (Materialise, Plymouth, Michigan), using a radio-density delineation range of -1024 to -300 Hounsfield units, and was complemented by clinically-monitored hand-editing of the selected pixels to ensure anatomic accuracy. The output STL (stereolithography) geometries were then spatially meshed on ICEM-CFD 2019 R3 (ANSYS Inc., Canonsburg, Pennsylvania) with minute volume elements. Therein, to confirm grid-independent solutions, established mesh-refinement protocols [28, 29] were followed such that each computational grid contained more than 4 million unstructured, graded, tetrahedral elements. To enable accurate tracking near tissue surfaces, further mesh refinement involved adding three prism layers at the cavity walls, with 0.1-mm thickness and a height ratio of 1.

2.2.2 Simulation of breathing transport and drug delivery

In this study, a male weighing 75 kg was identified as subject 1, and a female weighing 75 kg was identified as subject 2. By utilizing this data, we can determine the inhalation rate for both subjects while breathing gently. According to Equation 1.1 and Equation 1.2, the inhalation rate for the male subject is 18.20 L/min, whereas the female subject's inhalation rate is 15.05 L/min.

Inhalation parameters for gentle-to-moderate breathing conditions were numerically replicated at 15 and 30 L/min [26]. The lower flow rate commensurate with resting breathing is dominated by viscous-laminar steady-state flow physics [2, 30, 31, 32, 33, 34]. The higher flow rate for moderately heavy breathing (e.g., during sniffs), however, triggers shear-induced [35, 36, 37, 38, 39, 40] flow separation from the tortuous cavity walls, resulting in turbulence [41, 42, 43, 44]. The latter was tracked through Large Eddy Simulation (LES), with sub-grid scale Kinetic Energy Transport Model [45] accounting for the small-scale fluctuations. The computational scheme on ANSYS Fluent 2019 R3 employed a segregated solver, with SIMPLEC pressure-velocity coupling and second-order upwind spatial discretization. Solution convergence was monitored by minimizing mass

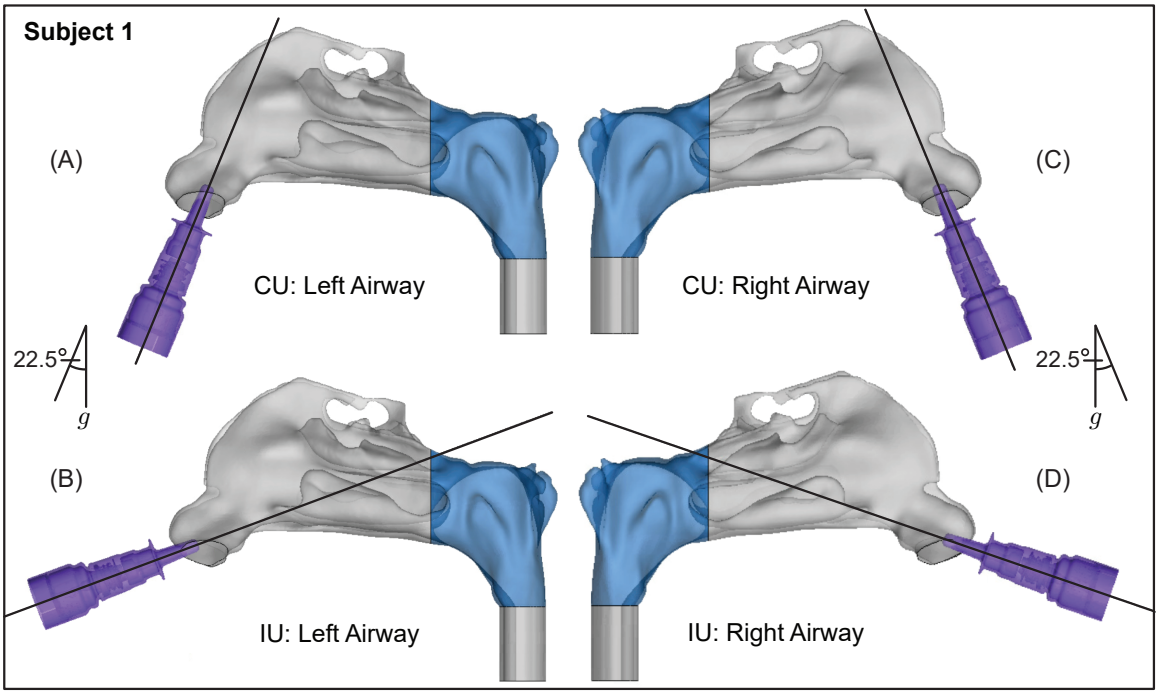

Figure 2.2: Spatial differences between the Current Use (CU) and Improved Use (IU) spray placement protocols, as visible sagittally in Subject 1. Nasopharynx is marked in blue, g points to the direction of gravity.

continuity and velocity component residuals, and through stabilizing mass flow rate and static pressure at airflow outlets (see the nasopharyngeal outlet location in Fig. 1.1). For the pressure gradient-driven laminar airflow solutions, the typical execution time for 5000 iterations was 2–3 hours with 4-processor based parallel computations operating at 3.1 GHz speed on Xeon nodes. Additionally, the LES computations each required a run-time of 1–2 days, for a pressure-driven simulated flow interval of 0.25 s, with a time-step of 0.0001 s. To realistically capture the continuum properties for inhaled warmed-up air transport inside the respiratory pathway, the air density and dynamic viscosity were set at 1.204 kg/m^3 and 1.825×10^{-5} kg/m.s, respectively. However, note the simulations did not incorporate any heat transfer effects. Spray dynamics against the ambient airflow was tracked via Lagrangian-based inert discrete phase simulations with a Runge-Kutta solver, with localized droplet clustering along intranasal tissues obtained through numerically integrating the transport equations that consider airflow drag, gravity, and other body forces relevant for small particulates, e.g., the Saffman lift force, and by implementing a no-slip trap bound-

ary condition on the cavity walls. Note that Brownian effects were neglected in view of the tracked droplet sizes. The drug formulation density was set to 1.5 g/mL, as a realistic estimate [46, 47]. All simulations released monodispersed inert drug droplets ranging in diameters from 1 – 24 μm, with 3000 monodispersed inert droplets being released during each iteration. The droplets were introduced into the airspace as a solid-cone injection emanating from a single source point where the spray nozzle is located, mimicking the action of a nasal spray; this method of release is referred to as a cone injection. Aptar Pharma's VP7, a commercially produced pharmaceutical nasal spray pump, with its accompanying dimension properties, such as plume angle and initial spray velocity, was used as an initial point of reference for the cone injections [48]. The droplets were given a starting velocity of 10 m/s [49] and a total non-zero mass flow rate of 1×10^{-20} kg/s for the streams in the spray cone. The plume angle (i.e., the half-angle at the hollow spray cone vertex) and the intranasal nozzle insertion depth were selected [2] to be 27.93° and 5 mm, respectively. Subsequently, by varying the spray direction – a new usage condition that would significantly augment droplet deposition at the target site was detected.

2.2.3 On how to hold the spray bottle

A key parameter for targeted delivery is the direction of the nasal spray axis, as the sprayed droplet trajectories are often inertia-dominated [2, 32, 50, 51]. Instructional ambiguities [52, 53] point toward a lack of definitive knowledge on the best ways to use a nasal spray device, with package inserts accompanying different commercial spray products often offering somewhat contrasting recommendations. There is, however, a consensus that the patient should tilt her/his head slightly forward while holding the spray bottle upright [52, 54]. There is an additional clinical recommendation [55] to avoid pointing the spray directly at the septum, which is the separating cartilaginous wall between the two sides of the nasal cavity. These suggestions were adopted in our standardization [2, 56] of the "Current Use" (CU) protocol for topical sprays. The digital airway models were inclined forward by an

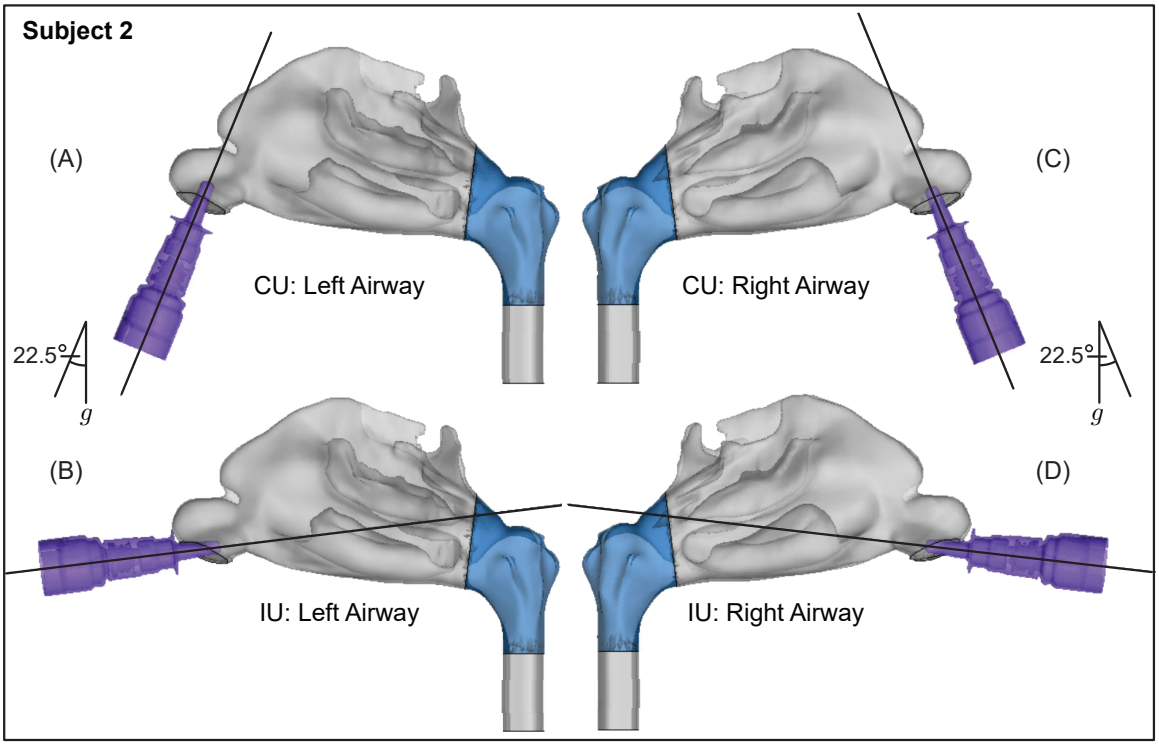

Figure 2.3: Spatial differences between the Current Use (CU) and Improved Use (IU) spray placement protocols, as visible sagittally in Subject 2. Nasopharynx is marked in blue, g points to the direction of gravity.

angle of 22.5°, and the vertically-placed upright [52] spray axis was aligned closer to the lateral nasal wall, at one-third of the distance between the lateral side and septal wall. Finally, the spray bottle was placed at the nostril to penetrate 5-mm into the airspace, to conform with the package recommendations of commercial sprayers [54] for a "shallow" intranasal nozzle placement.

While the CU protocol would provide the acceptable state-of-art for targeted drug delivery with nasal sprays, the key focus of this study was to re-examine the angle(s) at which the spray is administered relative to the nasal geometry ("spray direction") to test alternate protocols that bear the promise to improve delivery of drugs at the nasopharyngeal infection site. Our earlier findings [2] showed that to target the clinical site of ostiomeatal complex, or OMC (a key target site for corticosteroid-based topical therapeutic management for chronic rhinosinusitis [2, 33] and allergic rhinitis [57]), the spray axis should be oriented to pass through the OMC itself. The inertial motion of the sprayed particulates

assists such a transport mechanism. Accordingly, to optimize the spray administration protocol in the current study, we oriented the nozzle such that the spray axis passes through the nasopharynx, and have named the strategy as "Improved Use", or IU protocol. When determining the IU direction, it was important to satisfy three conditions as a way of ensuring the optimal placement of a nasal spray for drug release: (i) the extended spray axis for the IU protocol must intersect the nasopharynx; (ii) the spray axis must not cut through the septal wall to conform with clinical safety; and (iii) the axis should intersect the lateral wall in the posterior part of the nasal cavity. See the cartoonized Fig. 2.1 for a broad-spectrum visual difference between the presently recommended CU and the to-be-tested IU protocols. Additionally, Figs. 2.2 and 2.3 depict the spatial distinctions in spray placement between the IU and CU protocols, in the two test subjects, as visible from the sagittal perspective.

2.2.4 Tolerance sensitivity analysis

Once the IU for an airway reconstruction was determined (following guidelines outlined in Section 2.2.3), an axis perturbation-based tolerance sensitivity study was performed to assess how far the user could deviate from the determined IU spray direction and still get comparable regional drug deposition results, or in other words how robust (or, on the contrary, user-sensitive) the chosen IU direction really is.

To generate the new perturbed axes in the *in silico* space, a 1-mm radius circle was created perpendicular to the perturbed direction either 5-mm or 10-mm away from the central point on the nostril plane of each model. The two different distances were chosen in order to test the sensitivity of the results at different perturbation levels. The 5-mm method was performed on the left nostril of the subjects, while the 10-mm method was performed on the right nostril. Five peripheral points equidistant from each other were then selected on the circle created. The axis formed between the centroid point on the nostril plane and the peripheral point on the circle determined the new perturbed direction. In all, five additional perturbed spray axis directions were created for each nostril, henceforth referred to as PD

1 – 5. For each new perturbed direction, the injection point was selected by measuring 5-mm from the centroid on the nostril plane, toward the nasopharynx. Each new identified PD axis satisfied the criteria developed to identify the IU direction, as described in Section 2.2.3, and drug delivery simulations were performed following the methods laid out in Section 2.2.2. The results of the tolerance simulations were analyzed for congruity using Pearson's correlation coefficient.

2.3 Results

2.3.1 Improved orientation of the spray axis for effective targeting

Airflow and droplet transport have been simulated for spray nozzle placement at the left and right nostrils of Subjects 1 and 2, under two standard inhalation rates (15 and 30 L/min), for drug droplet diameters 1 – 24 μm, and for spray directions as per the "Current Use" (or, CU) and "Improved Use" (or, IU) protocols. See Fig. 2.1 for the respective spray usage protocol visuals, and also Section 2.2.3. In all eight cases, the IU direction of the spray axis results in higher deposition at the nasopharynx in comparison to the CU protocol (see Fig. 2.4). For instance, if we examine the deposition trends for spray administration through the right nostril of Subject 2 for the laminar regime inhalation (i.e., at 15 L/min), the peak nasopharyngeal deposition for IU is 46.5% for 13 μm drug droplets (Fig. 2.4(h)), while the peak deposition for CU is only 0.53% for 14 μm drug droplets (see again Fig. 2.4(h) and the corresponding zoomed-in visual for the CU delivery trends in Fig. 2.4(k)). The nearly hundred-fold increase in targeted deposition is remarkable and is achievable simply by re-orienting the spray axis from CU to IU.

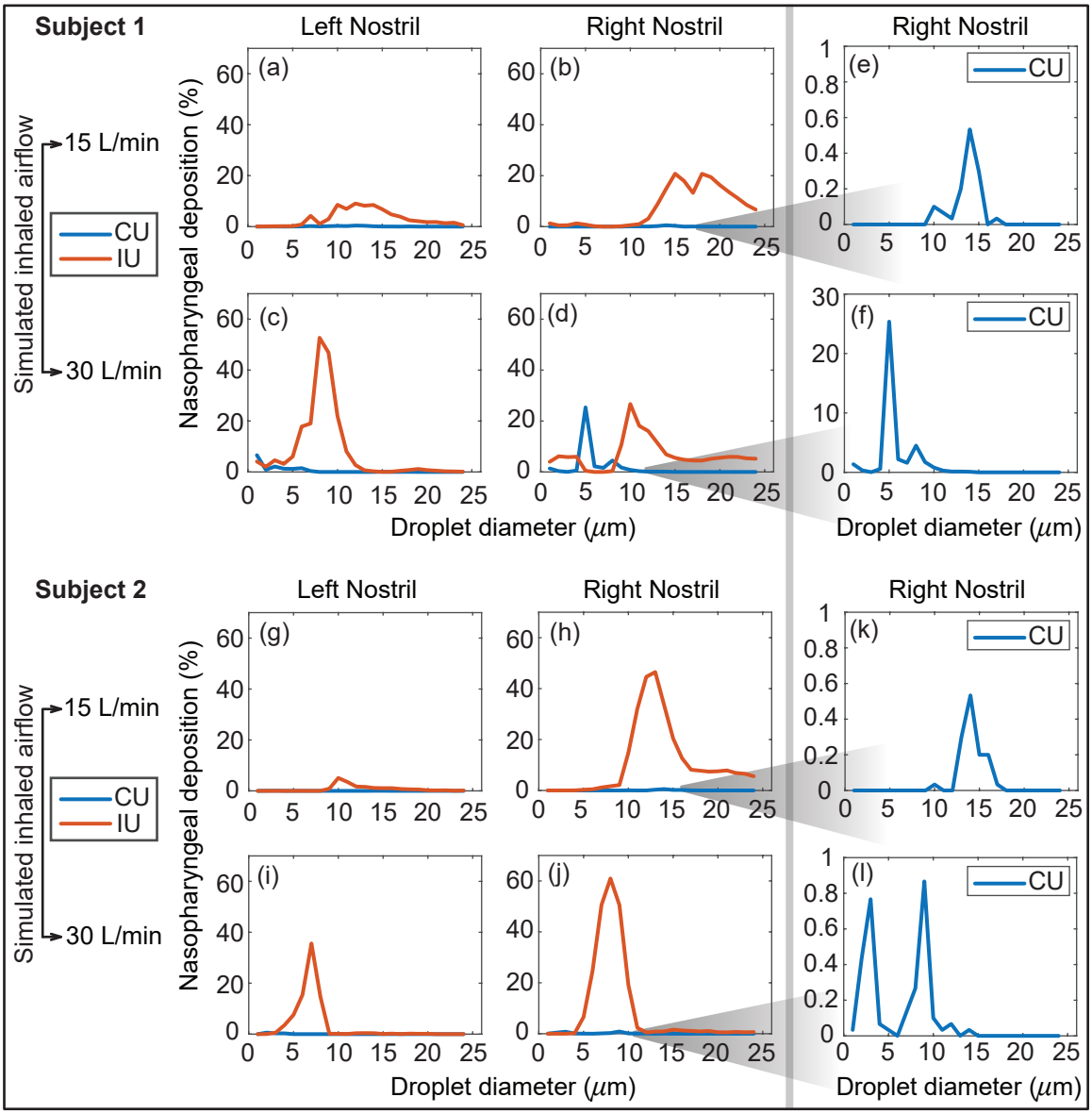

Figure 2.4: Panels (a) – (d) show the comparison of the regional deposition trends at the nasopharynx of Subject 1, for the IU and CU protocols, with monodispersed conical injections. The rows (a) – (b) are for 15 L/min inhalation; rows (c) – (d) are for 30 L/min inhalation. Panels (e) – (f) depict the representative zoomed-in trends for nasopharyngeal deposition with the CU protocol, on administering the spray through the right nostril of Subject 1. Similarly, panels (g) – (j) show the comparison of the regional deposition trends at the nasopharynx of Subject 2, for the IU and CU protocols. The rows (g) – (h) are for 15 L/min inhalation; rows (i) – (j) are for 30 L/min inhalation. Panels (k) – (l) depict the representative zoomed-in trends for nasopharyngeal deposition with the CU protocol, on administering the spray through the right nostril of Subject 2. The IU trend lines are marked in red; the CU trend lines are in blue. The reader should note the abbreviated vertical range on the (e) – (f) and (k) – (l) plots, prompted by the 2 orders-of-magnitude smaller deposition efficiency with CU.

2.3.2 Assessing sensitivity to IU perturbations

The variation of the nasopharyngeal deposition percentages over the assessed droplet size range (1 – 24 μm) was compared between that of the IU protocol and each of the perturbed

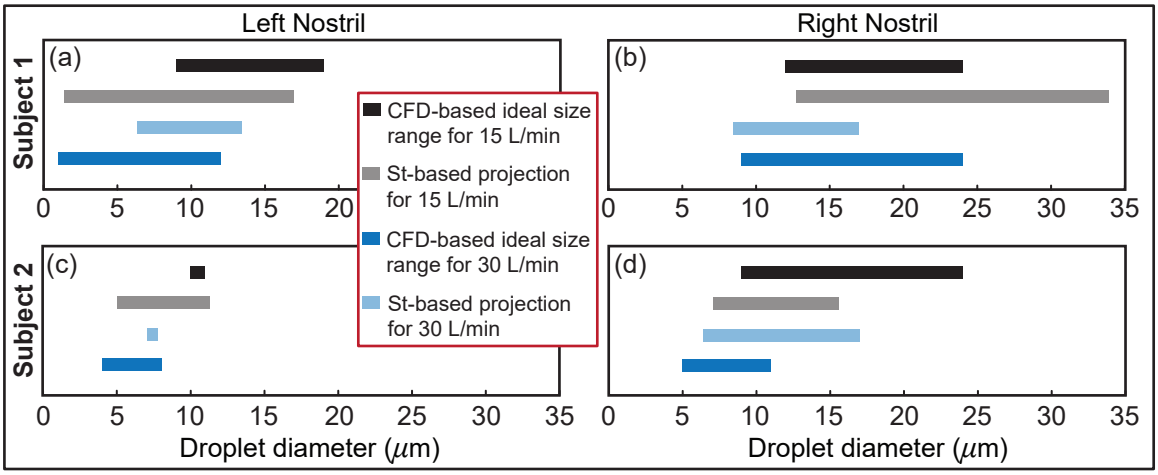

Figure 2.5: Panels (a) – (b) for Subject 1 and panels (c) – (d) for Subject 2 visually depict the Stokes number (St)-based projections of droplet size ranges for at least 2% targeted deposition at the nasopharynx. The directional change of the St-projected ranges along the number scale agrees with the corresponding CFD-based "ideal" droplet size ranges in all the test cases, except in one trivial outlier: see panel (b), where the maximum ideal size limits at both 15 and 30 L/min are 24 μm; the St-projected maximum ideal droplet size for 30 L/min is, however, 33.94 μm.

direction (PD) data, *viz.* PD 1 – 5. The PD spray orientations were obtained by slightly perturbing the IU direction; see Section 2.2.4 for details. Pearson's correlation coefficient was comfortably greater than 0.5 for nearly every such comparison (see Fig. 2.6), showing a high degree of linearity between the perturbed directions and the IU protocol in terms of the ranked order of the nasopharyngeal deposition efficiencies exemplified by the tested spray droplet sizes. Moreover, the p-value associated with each correlation was much lower than the significance level of ~ 0.05. This indicates that there is a statistically significant correlation between the simulation results on the targeted nasopharyngeal drug delivery for the IU and the perturbed directions. Physically, the satisfactory correlation between IU and PD 1 – 5 establishes the robustness of the IU spray protocol to user subjectivities.

2.3.3 Verification of optimal droplet sizes through scaling analysis

The droplet size ranges that registered peak nasopharyngeal deposition under each inhalation condition were further analyzed and validated for reliability, through a Stokes number-based scaling analysis [58]. The Stokes number (St), a ratio of the local transient inertia

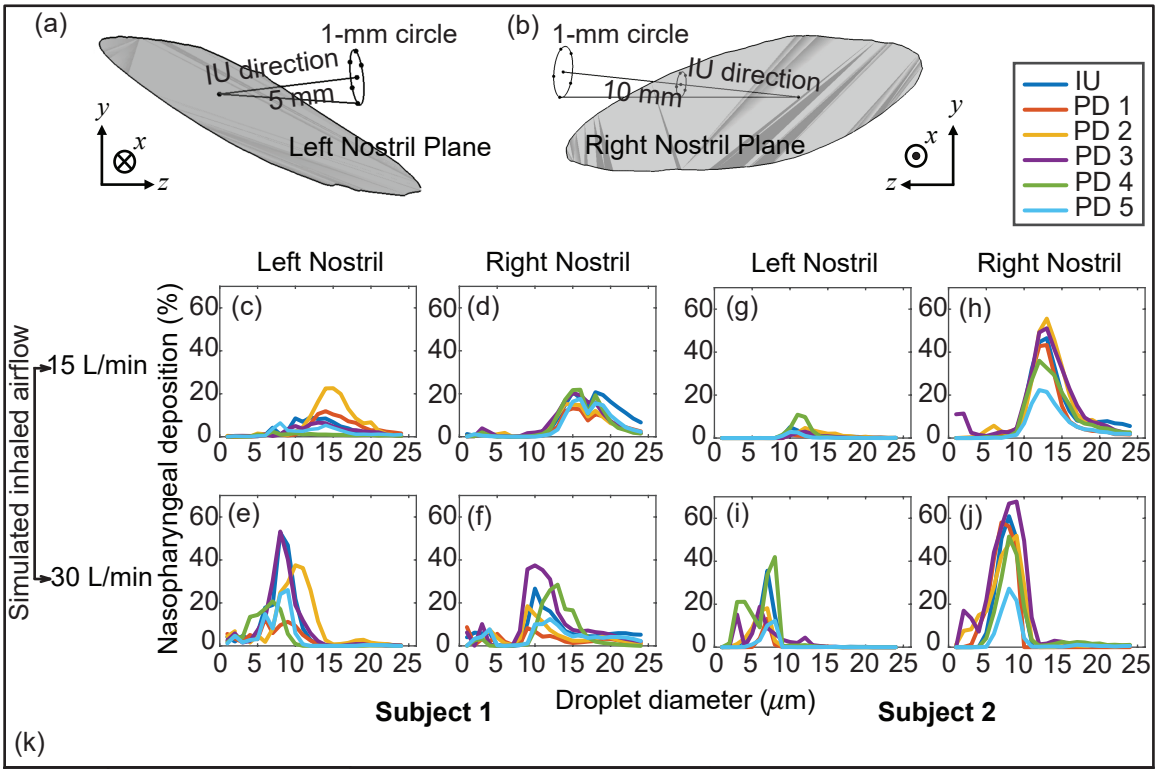

Model	Simulation Case	Pearson's Correlation Coefficient (r)					p-value associated with correlation				
		PD 1	PD 2	PD 3	PD 4	PD 5	PD 1	PD 2	PD 3	PD 4	PD 5
Subject 1	Left Nostril Administration 15 L/min Inhalation	0.6805	0.6745	0.9176	0.6155	0.6620	2.53E-04	3.01E-04	2.78E-10	1.37E-03	4.26E-04
	Right Nostril Administration 15 L/min Inhalation	0.9526	0.8795	0.8469	0.8769	0.9580	7.43E-13	1.52E-08	1.80E-07	1.89E-08	2.01E-13
	Left Nostril Administration 30 L/min Inhalation	0.8191	0.6122	0.9725	0.5525	0.9577	9.87E-07	1.48E-03	2.07E-15	5.12E-03	2.22E-13
	Right Nostril Administration 30 L/min Inhalation	0.4607	0.7348	0.8711	0.5499	0.8029	2.35E-02	4.33E-05	3.06E-08	5.37E-03	2.34E-06
Subject 2	Left Nostril Administration 15 L/min Inhalation	0.9549	0.6518	0.7115	0.7296	0.9342	4.33E-13	5.58E-04	9.67E-05	5.21E-05	2.54E-11
	Right Nostril Administration 15 L/min Inhalation	0.9848	0.9629	0.9523	0.9805	0.9939	3.24E-18	5.32E-14	8.03E-13	4.77E-17	1.50E-22
	Left Nostril Administration 30 L/min Inhalation	0.9348	0.8904	0.5591	0.7552	0.8534	2.29E-11	5.66E-09	4.51E-03	1.99E-05	1.16E-07
	Right Nostril Administration 30 L/min Inhalation	0.9413	0.9512	0.9387	0.9877	0.9797	7.53E-12	1.02E-12	1.18E-11	3.05E-19	7.44E-17

Figure 2.6: Panels (a) and (b) illustrate the *in silico* detection of the perturbed spray directions (PD), deviating slightly from the IU axis. The direction vectors are from the centroid of the nostril plane to the points lying on a 1-mm circle that is 5 mm and 10 mm (respectively for the left and right nostril placement) from the nostril plane centroid (see Section 2.2.4 for associated details). Panels (c) – (f) for Subject 1 and panels (g) – (j) for Subject 2 compare the respective nasopharyngeal deposition trends for PD 1 – 5 directions, with respect to that of the "Improved Use" (IU) protocol. The top row is for 15 L/min inhalation; the bottom row is for 30 L/min inhalation rate. Clustering of the plots signifies robustness of the IU usage parameters; in other words, the IU protocol is satisfactorily less sensitive to user subjectivities. (k) Statistical tests are performed to check the correlation between the regional deposition efficiencies (for the discrete drug droplet sizes 1 – 24 μm) at the nasopharynx for the perturbed spray directions (i.e., PD 1 – 5), when compared to the nasopharyngeal deposition efficiencies for the same droplet sizes with the IU protocol. The tabulated data includes the Pearson's Correlation Coefficients (and associated p-values, with $\alpha = 0.05$).

over viscosity, is mathematically defined as [51]

$$\mathrm{St} = \frac{U\,\rho_{\mathbb{D}}\,\mathbb{D}^2\,C_c}{18\,\mu\,d}, \tag{2.1}$$

where U for the present system is the airflow rate divided by flux area, $\mathbb{D}$ is the droplet diameter, $\rho_{\mathbb{D}}$ is the material density of the inhaled droplets, C_c is the Cunningham slip correction factor, μ is the dynamic viscosity of the ambient medium (i.e., air), and d represents the characteristic diameter of the flux cross-section. Now, with all other flow and morphological parameters staying invariant, Equation 2.1 directly leads to the following scaling law:

$$\frac{\mathbb{D}_2}{\mathbb{D}_1} = \sqrt{\frac{Q_1}{Q_2}}. \tag{2.2}$$

Herein $(Q_i, \mathbb{D}_i)$ are different inhaled airflow rate and sprayed droplet size pairings. Let us now consider a representative example, say the right nostril spray administration in Subject 2. For at least 2% nasopharyngeal deposition, the computationally predicted ideal droplet size range during 30 L/min inhalation is $[\mathbb{D}_{\text{min}},\ \mathbb{D}_{\text{max}}] = [5,\ 11]$ μm. Equation 2.2 can consequently help us to project the corresponding ideal size range at the lower inhalation rate of 15 L/min. If the to-be-projected droplet size range that would generate peak nasopharyngeal deposition during the 15 L/min inhalation is represented by $[\mathbb{D}'_{\text{min}},\ \mathbb{D}'_{\text{max}}]$ in μm, then

$$\frac{\mathbb{D}'_{\text{min}}}{5} = \frac{\mathbb{D}'_{\text{max}}}{11} = \sqrt{\frac{30}{15}}. \tag{2.3}$$

This results in $\mathbb{D}'_{\text{min}} = 7.07$ μm and $\mathbb{D}'_{\text{max}} = 15.56$ μm. Despite the simplicity of this scaling analysis, the computationally identified range 9 – 24 μm for the same breathing conditions hence follows the same trend on the number scale, in terms of the respective directional variations from the extremal limits of $[\mathbb{D}_{\text{min}},\ \mathbb{D}_{\text{max}}]$. Fig. 2.5(d) visually illustrates this specific example; see the remaining panels in Fig. 2.5 for all the other test cases. The directional change of the extremal limits for the St-projected ideal droplet size ranges remarkably agrees with the corresponding CFD-based size ranges in all cases, except in one trivial outlier: see panel (b) in Fig. 2.5 for Subject 1's right nostril, there the droplet size limits for at least 2% nasopharyngeal deposition with both 15 and 30 L/min inhalation rates

are 24 μm; the St-projected maximum ideal droplet size for 30 L/min, however, comes out to be 33.94 μm.

2.3.4 Generic ideal droplet size range for targeted delivery

Droplet diameter range of 7.375 — 16.625 μm, or more practically $\sim 7 - 17$ μm, is found most conducive for targeted nasopharyngeal delivery with the IU spray protocol, considering a 2% cut-off for deposition efficiency of the tracked monodispersed droplet cluster of each size. The limits of the generic ideal size range are obtained by respectively calculating the mean of the CFD-predicted minimum and maximum droplet diameters plotted in solid black and dark blue in Fig. 2.5; the averaging incorporated the droplet size data from all the eight test cases.

2.3.5 Estimation for active pharmaceutical ingredients delivery for sample over-the-counter spray products

To illustrate the practicality of our modeling approach in assessing drug therapeutic efficacy, let us now consider the experimental testing data of the spray products reported in Chapter 3 Section 3.1.1. The averaged estimates for the spray weight administered from each pump of a spray were 104.51 mg for Flonase^{TM} (Fluticasone Propionate) and 97.64 mg for Nasacort^{TM} (Triamcinolone Acetonide).

Based on our simulation data and by imposing the droplet size distribution measured for Flonase^{TM}, the mean nasopharyngeal delivery during each spray pump was 1.9187 mg for the IU protocol and 0.0495 mg for the CU protocol. Subsequently, assuming an API concentration of 50 mcg/100 mg of formulation [59] results in 0.96 mcg API delivery at the nasopharynx during the IU protocol, with direct inhalation. The corresponding number for the CU protocol with Flonase^{TM} is 0.025 mcg, hence remarkably lower than the IU performance. Subsequently, with the droplet size distribution for Nasacort^{TM}, our simulations

result in 1.8450 mg mean nasopharyngeal delivery during each spray pump with the IU protocol. The corresponding number with the CU protocol is 0.0482 mg. Hence for Nasacort™ which presents an API concentration of 55 mcg/110 mg of formulation [60], the mean API mass delivered at the nasopharynx through direct inhalation would be 0.92 mcg for IU and 0.024 mcg for CU.

Chapter 3

Experimental validation of computational nasal delivery results

3.1 Methods

3.1.1 Experimental validation of computationally predicted spray performance

To extrapolate to real-world spray performance that could be projected from the *in silico* framework, we linked the computationally predicted nasopharyngeal droplet deposition efficiencies with the size distribution of droplets (see Fig. 3.1) in two existing over-the-counter spray products – thus assessing the expected deposition at the nasopharynx with a typical nasal spray. Specifically, measured distributions for Flonase™ (Fluticasone Propionate) and Nasacort™ (Triamcinolone Acetonide), both of which are commonly prescribed medications that are commercially available, were used. Four units of each product were tested at Next Breath, an Aptar Pharma company (Baltimore, MD, USA). The team measured the plume geometry through a SprayVIEW® NOSP, which is a non-impaction laser sheet-based instrument. With the droplet sizes in a spray shot following a log-normal distribution, the droplet size distribution (where droplet diameters are represented by x) can be framed as a

probability density function [61]:

$$m(x) = \frac{1}{\sqrt{2\pi}x \ln \sigma_g} \exp\left[-\frac{(\ln x - \ln x_{50})^2}{2(\ln \sigma_g)^2}\right]. \tag{3.1}$$

Here the mass median diameters (alternatively, the geometric mean diameter [51]) for Flonase™ and Nasacort™ were respectively: $x_{50} = 37.16$ μm and 43.81 μm; the corresponding geometric standard deviations were respectively: $\sigma_g = 2.080$ and 1.994. The latter statistically quantify the measured range of the droplet size data. Note that the measurements were also collected with and without a saline additive in the sprayer, with the tests returning similar droplet size distributions. The reader is referred to our previous publications [2, 32] for additional details.

In order to validate and generalize the computational predictions obtained for real sprays, we conducted 20 physical injection experiments using a 3D-printed airway cavity of a different subject, Subject 3 (a 41-year-old male; the corresponding imaging data had a CT-slice resolution of 0.352 mm) that closely mimics the anatomical structure of the human airway. Printing of the related anterior soft plastic part on a Connex3™ 3D printer was carried out using polymer ink-jetting process on Tangogray FLX950 material, approximately mimicking the material properties of the external nares and the internal tissues and cartilages. The 3D-printed cavity extended until just before the nasopharynx, allowing us to measure the volume of solution that would reach the nasopharyngeal walls. Subject 3 was held upright and injected with 10 ml of dyed water solution for each of

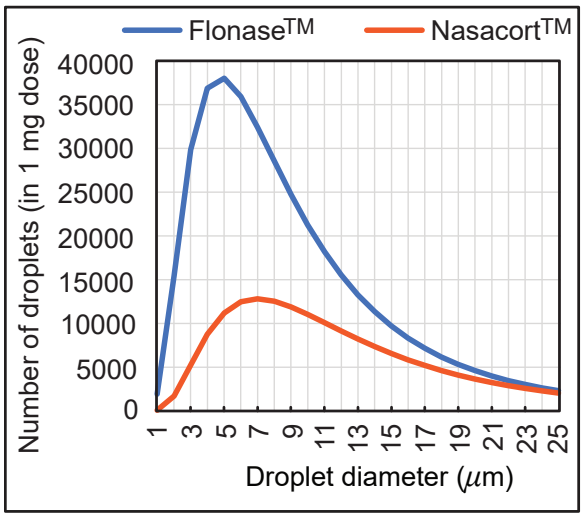

Figure 3.1: Observed distribution of droplet sizes in 1-mg sprayed mass from over-the-counter Flonase™ (Fluticasone Propionate) and Nasacort™ (Triamcinolone Acetonide) spray products, over the test size range of $\sim 1 - 24$ μm used for *in silico* tracking. Note that rigorous numerical testing for droplets > 24 μm clearly show [1, 2] that they would mostly deposit along the anterior nasal cavity and will largely miss the posterior target site of the nasopharynx.

the 20 runs. The injection was administered horizontally (as much as possible) and inserted at a shallow depth of 5 mm inside the airspace to emulate the "Improved Use" (IU) method for determining the solution volume that reaches the nasopharyngeal walls. To replicate the "Current Use" method, the injector was held vertically. Any discharge from the front of the nose was collected separately to ensure that it did not affect the measurement of the penetrating solution. See Fig. 3.2(c)-(d) for photographic representations of the 3D-printed soft nose used in the experiments.

3.2 Results

3.2.1 Comparison of the *in silico* findings to physical experiments

Panel (a) in Fig. 3.2 portrays the order-of-magnitude improvement in targeted drug deposition at the nasopharynx (with the IU protocol over the CU protocol), when taking into account the droplet size distributions [2, 32] in real over-the-counter spray products, *viz.* Flonase™ and Nasacort™, in an administered shot. See Section 3.1.1 for the related study methods. Considering all the test cases, the average IU-over-CU improvement for the two chosen spray products, as projected from the CFD simulations, was 2.117 orders-of-magnitude with a standard deviation of 0.506 orders. The physical experiments in Subject 3 show a comparable improvement in nasopharyngeal delivery, by 2.215 orders-of-magnitude, with a standard deviation of 0.016 orders. Panel (b) in Fig. 3.2 plots the experimental measurements. Hence, the computational predictions differ from the *in vitro* data by less than 5%, thereby lending robust support to the implemented *in silico* framework.

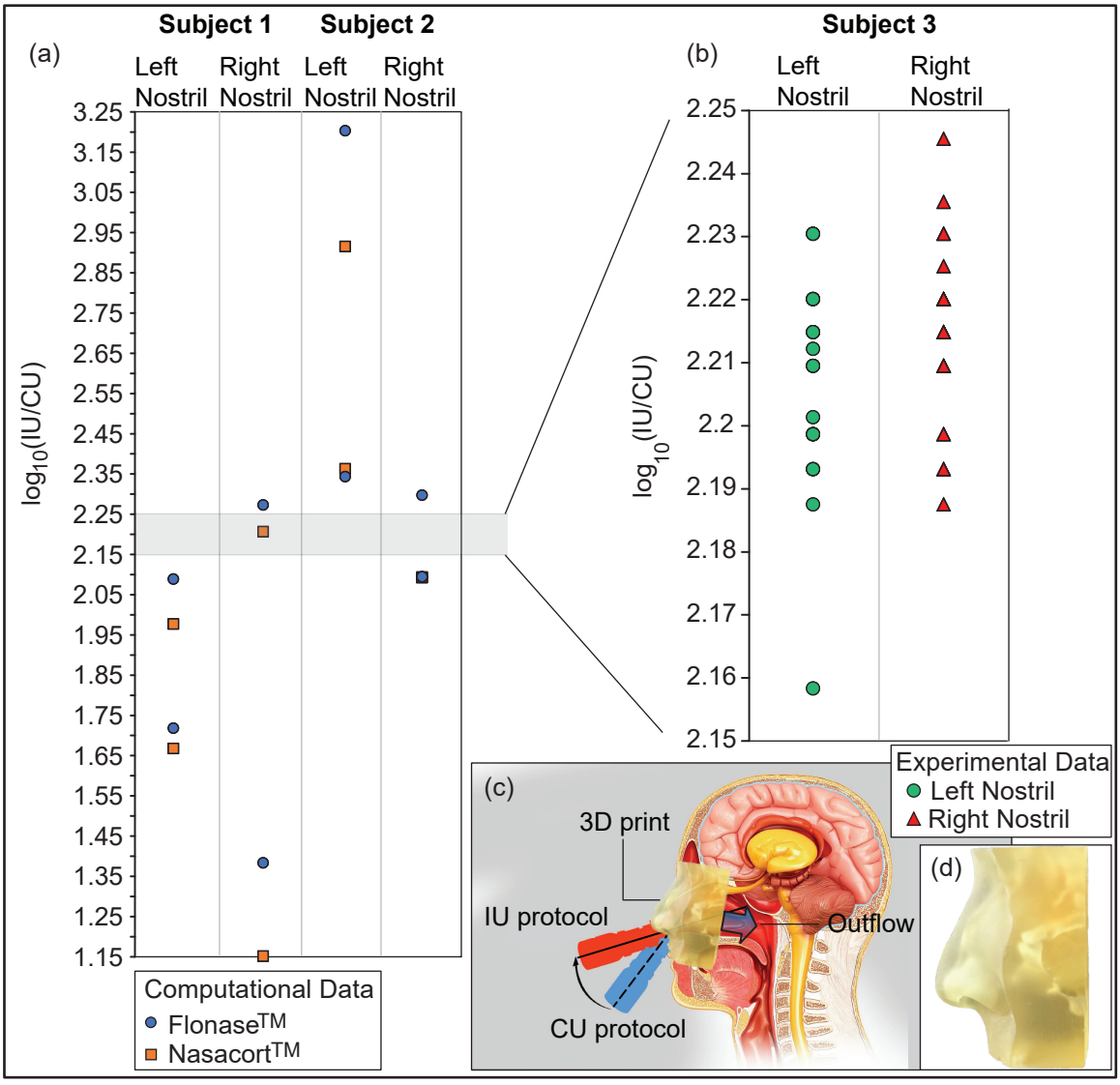

Figure 3.2: Experimental validation – Panel (a) shows the order-of-magnitude IU-induced improvement in drug mass deposits at the nasopharynx of Subjects 1 and 2 (when compared to the CU delivery numbers), while considering the droplet size distribution in each administered shot of two common over-the-counter spray products: Flonase™ and Nasacort™. Panel (b) shows the measurements from a set of physical experiments with sprayed watery solution in a different Subject 3. As an indicator for agreement between the computational and experimental projections, the vertical range in (b) is a medial subset of that in (a). Note that several data-points roughly superimposed over each other, in both (a) and (b). Panel (c) presents a cartoon of the experimental setup. A separate inset visual for the 3D-printed soft nose, with realistically pliable external nares, is shown in panel (d). Underlying cartoon illustration in panel (c) has been prepared by the Dr. Ferrer Biopharma (Hallandale Beach, FL) graphics design team.

3.3 Future work

I constructed an experimental setup in our laboratory to conduct precise angle experiments. To achieve accurate fixation of the nasal sprayer for the test angles, we utilized an adjustable angle hinge connector with a 0.75 inch diameter. A standard burette holder with clamps

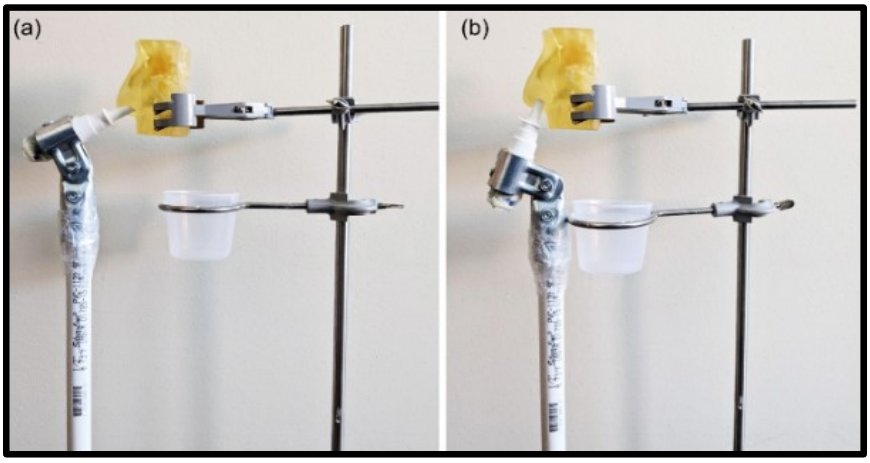

Figure 3.3: (a) Spray administration into an anatomic 3D-printed nose cast at approximately $15 - 18°$ to the horizontal. (b) Spray administration into the 3D-printed nose cast at $67.5°$ to the horizontal to replicate the currently prescribed spray protocol. Courtesy: Setup is prepared in collaboration with Abir Malakar (Graduate Student, Basu Lab, South Dakota State University)

was also used to hold the 3D model in place and collect the output solution that reaches the nasopharyngeal walls.

Fig 3.3 represents the nasal drug delivery process using a Pharma Quality Nasal Pump sprayer manufactured by Dr. Ferrer Biopharma. The physical spray tests were designed to evaluate drug penetration for two distinct nozzle orientations: (a) an angle of approximately $15 - 18°$ to the horizontal and a shallow insertion depth of 5 mm inside the airspace, which aligns with our recent in silico findings on enhanced usage protocols to target drug delivery at key infection and inflammation sites along the airspace, such as the nasopharynx for viral infections and the ostiomeatal complex for complications like chronic rhinosinusitis; (b) an angle of $67.5°$ to the horizontal and a shallow insertion depth of 5 mm inside the airspace, which replicates the schematic usage instructions of over-the-counter nasal spray products.

Chapter 4

Numerical modeling of airborne respirators infection onset

4.1 Overview

The nasopharynx is the primary site for SARS-CoV-2 infection. In this paper [62], a numerical framework was designed to identify the optimal droplet size range for nasopharyngeal infection. In my study of numerical modeling of airborne respirators' infection onset, I used the smallpox virus to create a framework that is applicable to all members of the poxvirus family. Notably, smallpox is transmitted through aerosolized saliva droplets, among other means, and is thus considered an anisotropic infection. This modeling framework is also applicable to the other members of the poxvirus family, such as monkeypox (MPX) and vaccinia virus (VarV).

4.2 Materials and Methods

4.2.1 Anatomic geometry reconstruction

The *in silico* upper airway geometries used in this study were digitally reconstructed from de-identified medical-grade CT imaging data derived from one healthy test subject. The use of the archived and anonymized medical records was approved with exempt status by the Institutional Review Board (IRB) of the University of North Carolina (UNC) at Chapel Hill,

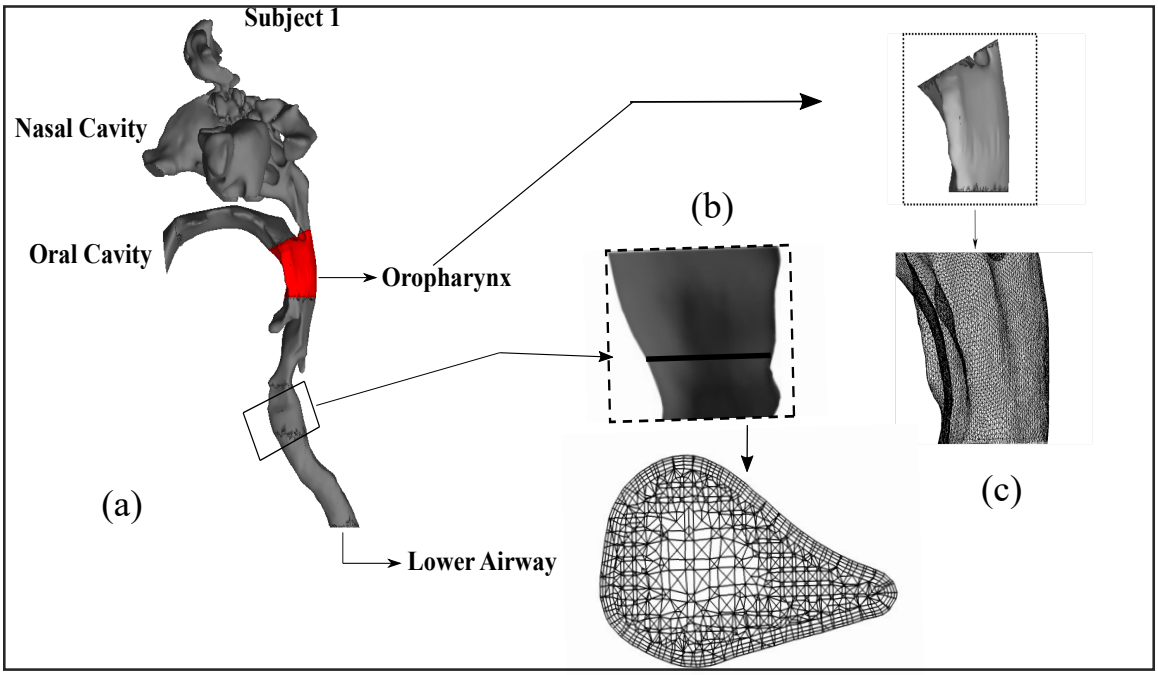

Figure 4.1: (a) Side view of airway model. (b) Enlarged view of glottic deposition, dark line at the level of the vocal folds. (C) Enlarged view of the oropharynx with prism layer mesh refinement elements. Oropharynx is marked in red in (a), (a–c) are generated using the software ICEM- CFD 3019 R3 (ANSYS Inc., Canonsburg, Pennsylvania;).

with the requirement of informed consent waived for retrospective use in computational research.

The reconstructed geometries were exported as STL (stereolithography) to ICEM-CFD 2019 R3 (ANSYS Inc., Canonsburg, Pennsylvania), and then meshed spatially into minute-volume elements. Therein, to confirm grid-independent solutions, established mesh-refinement protocols [28, 29] were followed such that each computational grid contained more than 7 million unstructured, graded, tetrahedral elements. To enable accurate tracking near tissue surfaces, further mesh refinement involved adding four prism layers at the cavity walls, with 0.1-mm thickness and a height ratio of 1.

4.2.2 Numerical simulation

Inhaled transport was studied through computational fluid dynamics (CFD) in Subject 1, for four different inhaled airflow rates, 15, 30, 55, and 85 L/min We have tracked all four airflow rates via Large Eddy Simulations (LES), with Kinetic Energy Transport Model as the sub-grid scale model [45]. Each LES computation required a run-time of 1–-2 days, for a simulated flow interval of 0.25 seconds, with the time-step at 0.0001 seconds. To account for the elevated temperatures inside the airspace, the simulations implemented an air density of 1.204 kg/m3, and 1.825 $\times 10^{-5}$ kg/m.s was used as the dynamic viscosity of air.

The simulations enforced the following boundary conditions: (1) zero velocity at the airway tissue interface, along with "trap" boundary condition for droplets, whereby the tracking of a droplet's transport would cease once it reaches the mesh layer lining the cavity walls; (2) zero pressure at inlets, which were the pressure-inlet zones in the simulations, with "reflect" boundary condition; and (3) a negative pressure at the outlet plane, which was the pressure-outlet zone, with "escape" boundary condition for the tracked particles, i.e., allowing for the outgoing particle to leave the test domain. To drive the 15 L/min air flux, the average inlet-to-outlet pressure gradient was -10.36 Pa, -38.2 Pa at 30 L/min, -114.32 Pa at 55 L/min, and -269.004 Pa at 85 L/min. The particle trajectories were tracked by Lagrangian-based discrete phase inert particle transport simulations against the ambient airflow, and additionally, the numerical scheme considered the effects of gravity and other body forces such as the Safman lift force exerted by a flow-shear field on small particulates moving transverse to the streamwise direction. In addition, a droplet size range with diameters 0.1 – 55 μm was considered large enough to neglect the effects of Brownian motion. For the numerical tracking, the initial mass flow rate of the inert droplets moving normal to the inlet planes into the nasal airspace was required to be non-zero and was set at 10^{-20} kg s^{-1}. The total number of monodispersed particles tracked for each tested size was 1660

when injected through the nostrils and 2185 when injected through the mouth. Finally, the particle density was assumed to be 1.3 g/ml, commensurate with the physical properties of environmentally dehydrated, often pathogenic, particulates [1, 63].

4.3 Results for smallpox

4.3.1 Droplet size range that targets the oropharynx and lower airway when entering through nostrils

The overall droplet size range of 8–27 μm registers the peak, in terms of the percentage of dehydrated droplets of each size that are deposited at the oropharynx of an exposed individual. The range is determined by a cut-off of at least 10% deposition for around 1660 tracked droplets of each size. Fig 4.2 shows the heat maps for oropharyngeal deposition (OPD) for different droplet sizes, during inhalation at the four tested airflow rates. The discrete droplet sizes, that were tracked, have been marked along the horizontal axis of the heat maps.

The overall droplet size range of $\leq$ 12 μ registers the peak, in terms of the percentage of dehydrated droplets of each size that are going to the lung through the lower airway of an exposed individual. The range is similarly determined by a cut-off of at least 10% deposition for around 1660 tracked droplets of each size. Fig 4.3 shows the heat maps for passing through the lower airway for different droplet sizes, during inhalation at the four tested airflow rates.

4.3.2 Droplet size range that targets the oropharynx and lower airway when entering through mouth

The overall droplet size range of 9–22 μm registers the peak, in terms of the percentage of dehydrated droplets of each size that are deposited at the oropharynx of an exposed indi-

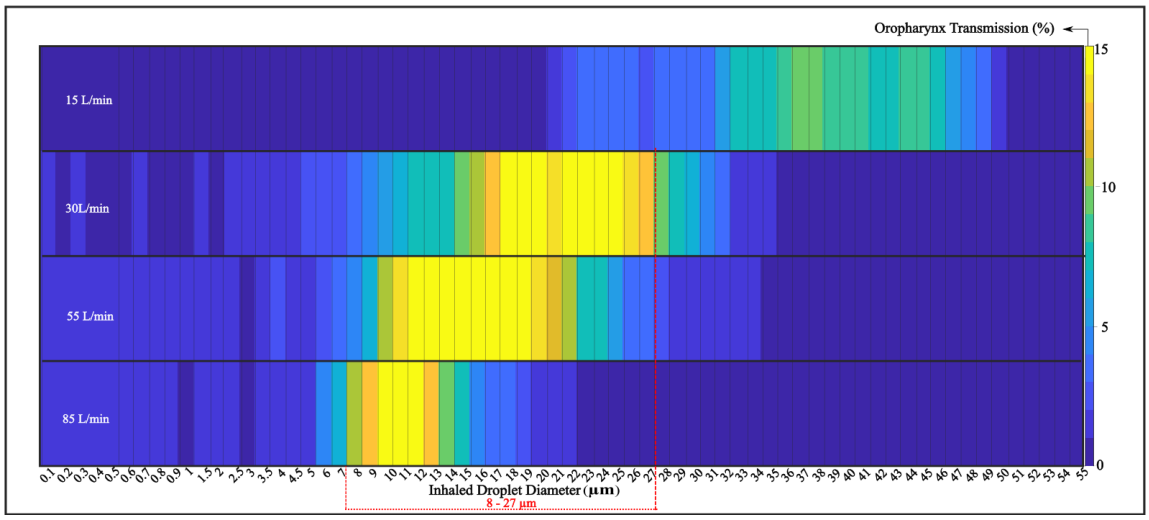

Figure 4.2: Visuals of heat-maps for inspiratory transmission trends in Subject 1, showing the percentage of droplets of each size undergoing oropharyngeal deposition (OPD). Data for different inhaled airflow rates are arranged along separate rows. Tracked droplet sizes are along the horizontal axis. OPD peaks for droplets sized between 8 and 27 μm in subject 1. 15, 30, 55, and 85 L/min are four inhalation rates.

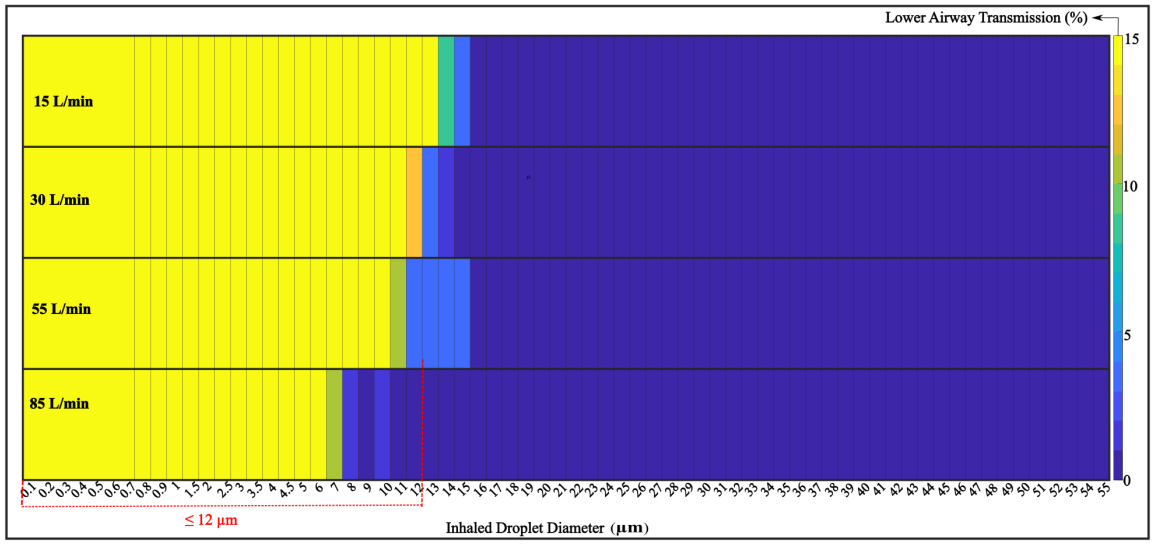

Figure 4.3: Visuals of heat-maps for inspiratory transmission trends in Subject 1, showing the percentage of droplets of each size undergoing lung deposition through the lower airway when injected through nostrils. Data for different inhaled airflow rates are arranged along separate rows. Tracked droplet sizes are along the horizontal axis. Lung deposition through the lower airway for droplets sized $\leq$ 12 μm in subject 1. 15, 30, 55, and 85 L/min are four inhalation rates.

vidual. The range is determined by a cut-off of at least 10% deposition for around 2185 tracked droplets of each size. Fig 4.4 shows the heat maps for oropharyngeal deposition (OPD) for different droplet sizes, during inhalation at the four tested airflow rates. The discrete droplet sizes, that were tracked, have been marked along the horizontal axis of the heat maps. The overall droplet size range of $\leq$ 14 μm registers the peak, in terms of the percentage of dehydrated droplets of each size that are going to the lung through the lower

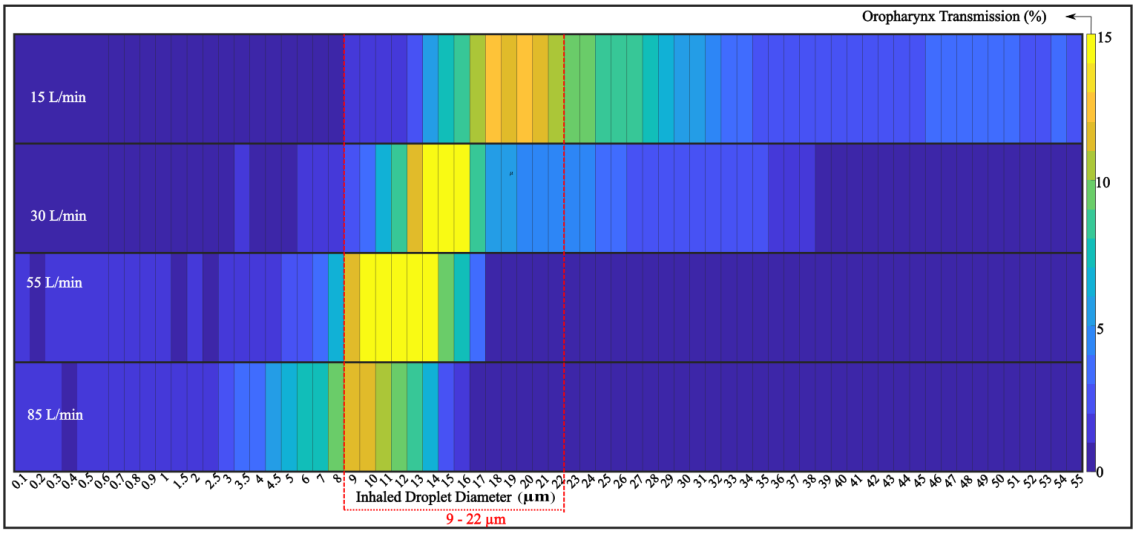

Figure 4.4: Visuals of heat-maps for inspiratory transmission trends in Subject 1, showing the percentage of droplets of each size undergoing oropharyngeal deposition (OPD) when injected through the mouth. Data for different inhaled airflow rates are arranged along separate rows. Tracked droplet sizes are along the horizontal axis. OPD peaks for droplets sized between 9 and 22 μm in subject 1. 15, 30, 55, and 85 L/min are four inhalation rates.

airway of an exposed individual. The range is similarly determined by a cut-off of at least 10% deposition for around 2185 tracked droplets of each size. Fig 4.5 shows the heat maps for passing through the lower airway for different droplet sizes, during inhalation at the four tested airflow rates.

4.3.3 On the smallpox infectious dose

The infectious dose is a fundamental virological measure quantifying the number of virions that can go on to start an infection. Theoretically, according to the independent action hypothesis, even a single virion can potentially establish an infection in highly susceptible systems. This study proposes a novel strategy for computational tracking and virological data, to estimate the infectious dose. Based on the oropharyngeal transmission trends for 1-hr exposure: the number of virions depositing at the susceptible individual's oropharynx is $4,000-40,000$ for both cases (injected through mouth and nostrils), considering the average DNA load in the carrier's sputum. On the contrary, the number of virions depositing at the susceptible individual's lung through the lower airway is $400-4000$ for both cases (injected through mouth and nostrils). We can say the lung (through the lower airway) is the most

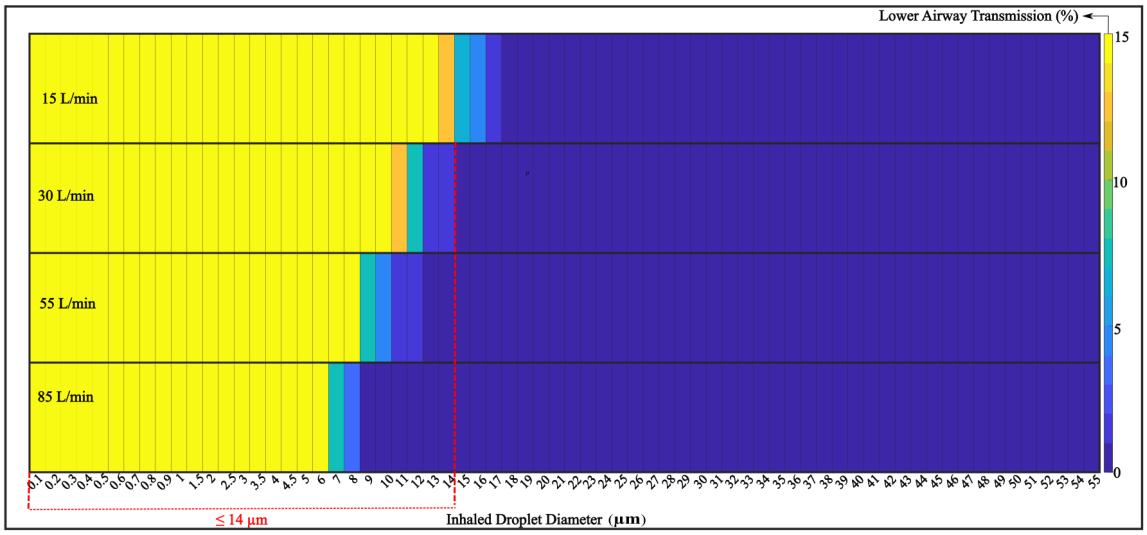

Figure 4.5: Visuals of heat-maps for inspiratory transmission trends in Subject 1, showing the percentage of droplets of each size undergoing lung deposition through the lower airway when injected through the mouth. Data for different inhaled airflow rates are arranged along separate rows. Tracked droplet sizes are along the horizontal axis. Lung deposition through the lower airway for droplets sized ≤ 14 μm in subject 1. 15, 30, 55, and 85 L/min are four inhalation rates.

dominant infectious site for smallpox than the oropharynx [64].

4.4 Extension of the approach for lower airway onset

While the nasopharynx is initially the dominant upper airway infection site for SARS-CoV-2, the physiologic mechanism launching the infection in the lower airway is still not well-understood. Based on the rapidity of infection progression to the lungs, it has been conjectured that the nasopharynx acts as the seeding zone for subsequent contamination of the lower airway via aspiration of virus-laden boluses of nasopharyngeal fluids. To examine the plausibility of this mechanism, we have computationally tracked the inhalation process in two anatomic airway reconstructions and have quantified the nasopharyngeal liquid volume transmitted to the lower airspace during each aspiration.

The extension of the approach for lower airway onset was published in 2021 in Rhinology online under the title “From SARS-CoV-2 infection to COVID-19 morbidity: an in silico projection of virion flow rates to the lower airway via nasopharyngeal fluid boluses”.

4.4.1 Materials and Methods

4.4.1.1 Frequency and quantification of pharyngeal aspiration

Aspiration (i.e. accidental suction of fluid and cells into the lungs) of upper airway secretions acts as a major carrier of pathogens to the lower airway, and the phenomenon, fortunately enough, has been studied in great detail over the last few decades. As reported in the late-1990s [11], aspirated pharyngeal liquid volume during sleep ranges from 0.011 ml to 0.129 ml, measured through tracking mildly-radioactive tracers after the subjects wake up. Further introspection of the published data indicates that the maximum data-point in the reported range is a statistical outlier. Including the maximum-reported volume in the analysis, the mean aspirated volume comes out to be 0.0345 ml and the median is 0.0215 ml. Excluding the outlier, the mean volume revises to 0.021 ml and the median volume adjusts to 0.020 ml. The study [11] was based on a total of 10 normal subjects. While evaluating swallowing mechanisms, it has been further comprehensibly reported [12] that for 5-ml bolus volumes, aspirations happen during 13% of swallows; and for 10-ml bolus volumes, aspirations happen during 11% of swallows. Boluses smaller than 10 ml are associated with silent aspiration [65] and presumably are the major sources of pathogen-carriers to the deep lungs, and with averaging the reported data for 5-ml and 10-ml volumes, 12% of the swallowing actions should result in aspiration. Finally, earlier findings [66] suggest that a typical person will swallow 500 – 700 times during a day and 24 times during sleep (assuming a standard eight-hour sleep cycle). These numbers thus indicate that a subject will aspirate approximately 12% of 500 – 700 times, i.e. 60 – 84 times during the day, and 12% of 24 times, i.e. approximately 3 times during sleep.

4.4.1.2 Development of anatomically realistic computational fluid mechanics models

Allometric relations [26] show that the minute inhalation is approximately 14.5 – 20.0 L/min for a 65-kg adult male and 8.8 – 22.4 L/min for a 65-kg adult female, both for gentle steady

breathing. For simplicity, as a stand-in for gentle inhalation [67, 68, 69, 70], this study simulates an airflow of 15 L/min; the process can be modeled using viscous-laminar steady-state flow physics schemes [2, 30, 31, 32, 33, 71, 72, 73, 74, 75]. We additionally noted that subjects with a proclivity to apnea are also prone to higher levels of aspiration [76] and for them, the inhaled air often disrupts into high-speed turbulent regimes. To account for such flow conditions, we have simulated a higher breathing rate of 55 L/min.

4.4.1.3 Anatomic airway reconstructions

The *in silico* anatomic geometries were reconstructed from medical-grade computed tomography (CT) scans sourced from existing de-identified imaging data from two CT-normal subjects. Use of the archived records was approved with exempt status by the Institutional Review Board of the University of North Carolina (UNC) at Chapel Hill, with the informed consent requirement waived for retrospective computational use. The test subjects include a 61-year-old female (named hereafter Subject 1) and a 37-year-old female (named as Subject 2), and a 24-year-old female (named Subject 3). Subjects 1 and 2 presented clinically normal CT scans, while Subject 3 had a post-FESS (Functional Endoscopic Sinus Surgery) airway with a diagnosed pre-procedural complication of Chronic Rhinosinusitis. As for imaging resolution, the CT slices were collected at coronal depth increments of 0.4 mm. The anatomic airspace was extracted from the scans over a delineation range of -1024 to -300 Hounsfield units, the process was complemented by careful hand-editing of the selected pixels for anatomic accuracy. This phase of digital reconstruction was carried out by processing the DICOM (Digital Imaging and Communications in Medicine) scans of the subjects' airways on the image processing software Mimics Research v18.0 (Materialise, Plymouth, Michigan). Subsequently, the reconstructed geometries were exported as STL (stereolithography) files to ICEM-CFD v15.0 (ANSYS Inc., Canonsburg, Pennsylvania) and therein were spatially meshed into minute volume elements. As per established mesh refinement protocols (e.g. see [28, 29] and more recently [34, 77]), each computational grid

in this study has more than 4 million unstructured, graded tetrahedral elements (namely 4.54 million in Subject 1, 4.89 million in Subject 2 and 4.05 million in Subject 3).

4.4.1.4 Simulating inhalation

Inhaled transport was studied through computational fluid dynamics (CFD) in the three meshed geometries (Subjects 1 – 3), for two different inhaled airflow rates, 15 and 55 L/min To track the 15 L/min flow, viscous-laminar steady-state simulations of the inhalation process were carried out using a segregated solver on ANSYS Fluent 2019 R3, with SIMPLEC pressure-velocity coupling and second-order upwind spatial discretization. We monitored the solution convergence by minimizing the mass continuity and velocity component residuals, and by stabilizing the mass flow rate and static pressure at the airflow outlets. For the pressure-driven flow solutions, typical run-time for 5000 iterations was 2–3 hours through 4-processor based parallel computations executed at 3.1 GHz speed on Xeon nodes. The higher flow rate of 55 L/min results in turbulence [41, 42, 43, 44, 78], which we have tracked via Large Eddy Simulations (LES), with Kinetic Energy Transport Model as the sub-grid scale model [45]. Each LES computation required a run-time of 1–2 days, for a simulated flow interval of 0.25 seconds, with the time-step at 0.0001 seconds. To account for the elevated temperatures inside the airspace, the simulations implemented an air density of 1.204 kg/m3, and 1.825 $\times 10^{-5}$ kg/m.s was used as the dynamic viscosity of air.

The following boundary conditions were enforced in the flow simulations: zero velocity (*no slip*) at the internal airway walls i.e. at the tissues and cartilages enclosing the airway; zero pressure at nostril openings, which acted as the pressure-inlet zones; and negative pressure at the airflow outlet at the base of the nasopharynx, which acted as the pressure-outlet zone. See Figure 1.1 for the relative locations of the anatomic regions.

4.4.1.5 Theoretical estimation of aspirated nasopharyngeal liquid volume

For an instantaneous pathogenic event such as pharyngeal aspiration, the transport of the nasopharyngeal liquids downstream to the lower airway can be mathematically described through a reduced-order mathematical model of steady unidirectional flow. With the assumption of axial symmetry in the airway conduit and *no slip* boundary condition at the walls, integrating the Navier-Stokes equation for momentum conservation results [79, 80, 81] in

$$\mathbb{Q} = -\frac{\pi \mathcal{R}^4}{8\mu} \frac{dp}{dz}, \tag{4.1}$$

where $\mathbb{Q}$ is the instantaneous aspirated volume, $\mathcal{R}$ is the hydraulic radius (cross-section of conduit divided by the perimeter at the nasopharyngeal base), μm is the sputum viscosity (quantified at 4.59 Poise for mucopurulent), and dp/dz is the spatial rate of pressure gradient in the streamwise direction. To adapt the formulation to the present problem, we have post-processed the simulations to extract the averaged wall pressure at the nasopharynx (p_n), since the bolus would typically arise from the shearing action along nasopharyngeal surfaces. We have also extracted the averaged pressure (p_o) at the outlet, located 20 mm (streamwise ΔZ, so as to ensure full flow development in the simulations) below the nasopharyngeal base. With $\Delta P = p_o - p_n$, the gradient rate dp/dz can therefore be approximated to simply $\Delta P/\Delta Z$.

4.4.2 Data on viral loading

SARS-CoV-2 is a *single-stranded* RNA virus (i.e. has single-stranded genomes made of ribonucleic acid), and the virological assessments [13] performed through PCR (polymerase chain reaction) with reverse transcription (RT-PCR) on the sputum (collected via nasopharyngeal swabs) of hospitalized COVID-19 patients indicate a mean viral load of $\mathcal{V}_{\text{ave}} = 7 \times 10^6$ RNA copies/ml of oral fluid. The peak load was $\mathcal{V}_{\text{peak}} = 2.35 \times 10^9$ copies/ml.

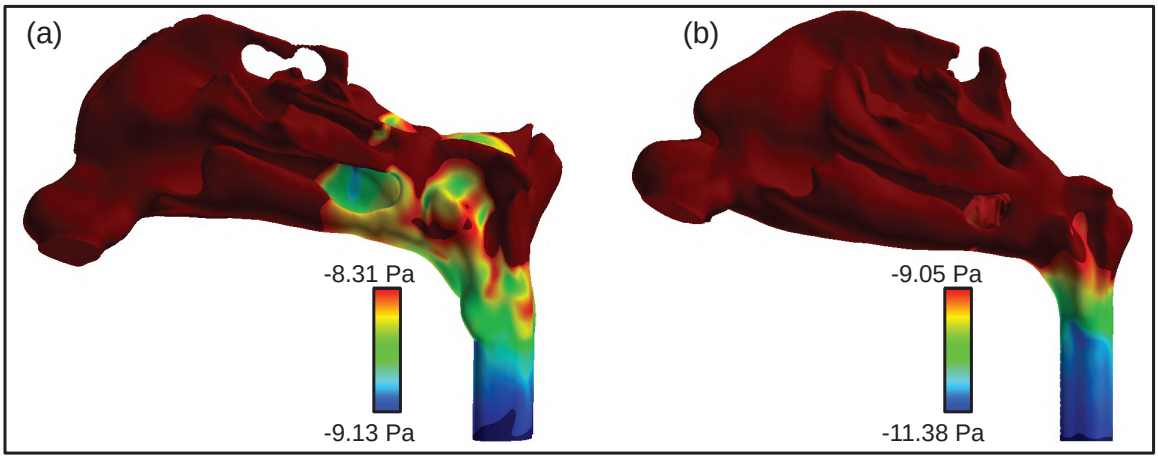

Figure 4.6: Panels (a) and (b) respectively depict the wall pressure maps in Subject 1 and Subject 2, for simulated inhalation of 15 L/min. Note that the pressure color-maps set the limiting contour colors at the respective p_n (averaged wall pressure at nasopharynx) and p_o (averaged pressure at outlet) values that are extracted from the simulated data in each case. The data post-processing is done on FieldView v18.0, under software license provided through the University Partners Program.

4.4.3 Results

4.4.3.1 Computational prediction of nasopharyngeal bolus volume

With inhalation simulated at 15 L/min: for Subject 1, ΔP was -0.82 Pa; for Subject 2, ΔP was -2.33 Pa (for contour maps, see Figure 4.6, Panels (a) and (b), and for subject 3, ΔP was -0.46 pa). The hydraulic radius in Subject 1 was 3.43 mm, i.e. $\mathcal{R} = 0.00343$ m; the hydraulic radius in Subject 2 was 3.06 mm, i.e. $\mathcal{R} = 0.00306$ m; and the hydraulic radius in Subject 3 was 4.08 mm, i.e. $\mathcal{R} = 0.00408$ m. Consequently using Equation 4.1, in Subject 1: the liquid bolus in each aspiration is $(\pi \times \mathcal{R}^4 \times |\Delta P|) \,/\, (8 \times 0.459 \times 0.02) = 4.86 \times 10^{-9}\,\text{m}^3 = 0.00486$ ml. Similarly in Subject 2: the liquid bolus volume ingested during each aspiration is 0.00874 ml; in Subject 3: the liquid bolus volume ingested during each aspiration is 0.00545 ml.

4.4.3.2 Estimation of aspiration frequency and validation of the computational predictions

Using the earlier observational data in the first paragraph of Section 4.4.1.1, in conjunction with the computed volumes in Section 4.4.3.1, the aspiration frequency during each sleep cycle is on the order of $0.021\,\text{ml}/0.00874\,\text{ml}$ and $0.021\,\text{ml}/0.00486\,\text{ml}$, or approximately 2 – 4 times. Calculations based on direct experimental observations provide an estimate of 3 aspirations during a sleep cycle (derived in the third paragraph of Section 4.4.1.1, using previous reports [12, 66]). The computational framework thus offers strong agreement with the direct experimental observations, providing a measure of validation for the underlying fluid dynamics framework.

4.4.3.3 Estimation of virion flow to the lower airway

Total number of aspirations of liquid boluses into the lower airway approximately ranges between 63 – 87 times in a day (see Section 4.4.1.1, note that the estimate includes the nocturnal aspirations during the subdued sleep phase). Based on the data from the current subjects in the numerical simulations (see Section 4.4.3.1), the total volume of aspirated liquid in a day is thus between 0.00486×63 ml and 0.00874×87 ml, or between 0.3 – 0.76 ml. With the virological data from Section 4.4.2, the number of virions penetrating into the lower airway, while suspended in nasopharyngeal fluid boluses, is therefore between $0.3 \times \mathcal{V}_{\text{ave}} = 2.1 \times 10^6$ and $0.76 \times \mathcal{V}_{\text{ave}} = 5.3 \times 10^6$, while considering the mean viral load. For peak viral load ($\mathcal{V}_{\text{peak}}$) in the sputum, the corresponding number of penetrating virions ranges over 7.1×10^8 – 1.8×10^9.

For 55 L/min inhalation: $\Delta P = -$ 8.41 Pa in Subject 1; -25.37 Pa in Subject 2; and $\Delta P = -$ 4.73 Pa in Subject 3. Therefore, the growth in ΔP is consistently 10-fold (when compared to the corresponding pressure differentials at 15 L/min, see Section 4.4.3.1 for details); the growth in virion transmission would also consequently be 10-fold.

Chapter 5

Machine Learning: A new tool for projecting airway transport

5.1 Overview

In this chapter, our focus is to answer this question– through Machine Learning (ML) techniques, can we use geometric features in anatomic scans to predict regional deposition along the human respiratory airspace? If yes, then this opens a new avenue for, e.g. targeted drug delivery predictions, without running cost-prohibitive numerical simulations.

5.2 Methods

5.2.1 Anatomic model reconstruction

Upper airway geometries were reconstructed *in silico* using de-identified medical-grade CT imaging data from 10 subjects. The use of the archived and anonymized medical records was approved with exempt status by the Institutional Review Board (IRB) of the University of North Carolina (UNC) at Chapel Hill, with the requirement for informed consent being waived in view of retrospective use for computational research. The anatomic airspaces were digitized using the image processing software Mimics Research v18.0 (Materialise, Plymouth, Michigan), with a radio-density delineation range of -1024 to -300 Hounsfield units, and were supplemented with clinically-monitored hand-editing of selected pixels to

ensure anatomic accuracy. To verify grid-independent solutions, established mesh refinement protocols [29, 82] were followed, resulting in over 4 million unstructured, graded, tetrahedral elements in each computational grid. To enable accurate tracking near tissue surfaces, additional mesh refinement included the addition of three prism layers with a 0.1-mm thickness and a height ratio of one at the cavity walls.

5.2.2 Simulation of breathing transport

On ANSYS Fluent 2019 R3, the computational scheme utilized a segregated solver with SIMPLEC pressure-velocity coupling and second-order upwind spatial discretization. Convergence of the solution was monitored by minimizing residuals in the mass continuity and velocity components, as well as by stabilizing the mass flow rate and static pressure at airflow outlets. The typical execution time for 1500 iterations of the pressure gradient-driven laminar airflow solutions was 0.5–1 hour using 4-processor parallel computations operating at 3.1 GHz on Xeon nodes. To accurately simulate the transport of warmed-up air along the respiratory pathway, the density and dynamic viscosity of the air were set to 1.204 kg/m^3 and 1.825×10^{-5} kg/m.s, respectively. Four different average inlet-to-outlet pressure and four different flow rate has been observed which drives to 16 data set for four different particle sizes and this gives 160 simulations data set for 10 geometries. Spray dynamics were tracked against ambient airflow using Lagrangian-based inert discrete phase simulations with a Runge-Kutta solver, with localized droplet clustering along intranasal tissues obtained by numerically integrating the transport equations that include airflow drag, gravity, and other body forces relevant for small particulates, such as the Saffman lift force, and by implementing a no-slip trap boundary condition on the cavity walls. Brownian effects were disregarded in light of the tracked droplet sizes. All simulations resulted in the formation of monodispersed inert drug droplets with diameters of 5, 10, 15, and 20 μm. The surface injection was used to inject the droplets into the airspace.

During simulations, the following boundary conditions were enforced: (1) zero velocity at

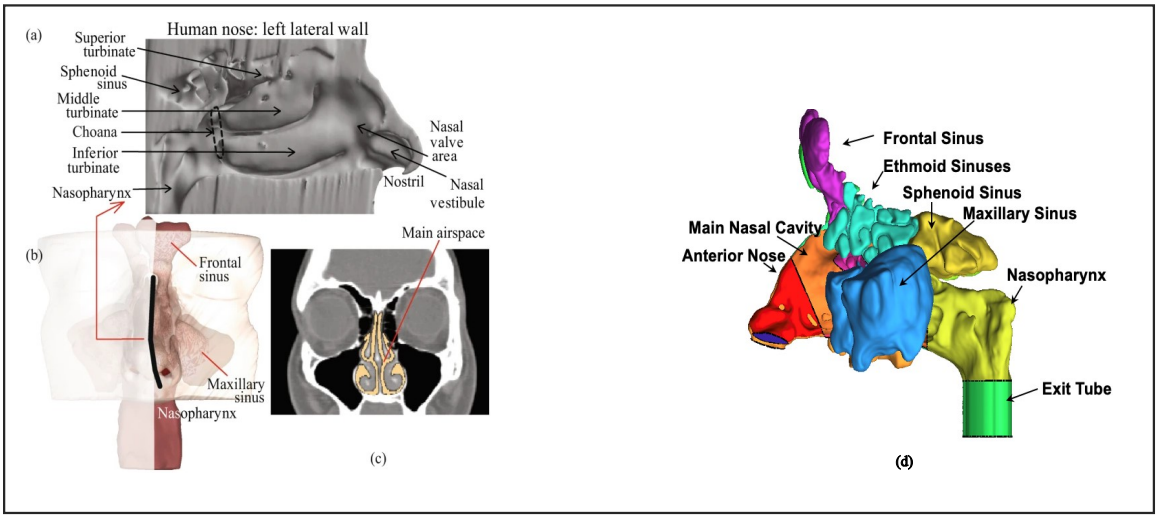

Figure 5.1: (a) Anatomic features inside a human nose, as viewed on an invasive cut-away. (b) Position of the cut-away section, marked by a dark line. (c) Representative coronal section, with the main nasal passage shown in a lighter color. (d) representative of anatomic features of the human nose, as viewed in 3D (adapted from Basu et al., 2020 [3]).

the airway tissue interface, along with "trap" boundary condition for droplets, wherein the tracking of a droplet's transport would cease once it landed on the walls; (2) zero pressure at the inlet, which were the pressure-inlet zones in the simulations, with "reflect" boundary condition; and (3) a negative pressure at the outlet plane, which was the pressure-outlet zone, with "escape" boundary condition for droplets, allowing for the outgoing droplet to escape. Inhaled droplet dynamics were tracked by Lagrangian-based discrete phase inert particle transport simulations in the ambient airflow; along with the effects of gravity and other body forces such as the Safman lift force exerted by a flow-shear field on small particulates moving transverse to the streamwise direction. For the numerical tracking, the initial mass flow rate of the inert droplets moving average to the inlet planes into the nasal airspace was required to be non-zero and was set at 10^{-20} kg/s, and the density of the material is 1.3 gm/ml [63].

5.2.3 Measurement of internal nasal geometry features

Measurements of nasal structural features were obtained using Ansys ICEM, version R21 (Ansys, 2021, Canonsburg, PA, USA). Specifically, eleven measurements made were for

each of the ten CT scans analyzed: left nostril height, right nostril height, left nostril circumference, right nostril circumference, coronal width, penetrative depth, the surface area of the nasopharynx, the volume of the nasopharynx, the surface area of the outlet plane, volume of the outlet plane, and total internal volume of the nasal cavity.

5.2.4 Applications of Machine Learning models

To address the question of whether machine learning can predict particle deposition at specific intranasal regions based on CFD inputs/outputs and nasal geometry measurements, 18 machine learning output types were developed, each predicting particle deposition at a different anatomical region of the nasal cavity. Figure 5.1 shows most of the regions of nasal airspace, and 18 regions have been named as output 1–18 in Table 5.1. The CFD parameters utilized were particle diameter, simulated pressure drop, outlet volume flow rate, and the number of particles tracked. For each model type, three different analyses were conducted: Analysis (i) with CFD parameters as models inputs; analysis (ii) with CFD parameters and nasal geometry measurements as models inputs; and analysis (iii) with CFD parameters and principal components of the nasal geometry measurements as model inputs. Multilayer perceptron, linear regression, and random forest machine learning algorithms were applied to these data to generate 54 models (18x3) using Waikato Environment for Knowledge Analysis (WEKA), version 3.8.6 [83, 84].

The performance of the machine learning predicted models was evaluated in WEKA by examining the correlation, root relative square error, and ZeroR model. The correlation between the predicted number of particles deposited and the number of particles over the dataset was calculated for each anatomical region. The root relative square error is relative to the result if a simple predictor, based solely on the average of the actual values, was used. The equation [85] of root relative square error (RRSE) is,

Output 1	Nasopharynx
Output 2	Lower Airway
Output 3	Left Ethmoid Sinus
Output 4	Left Maxillary Sinus
Output 5	Right Frontal Sinus
Output 6	Right Ethmoid Sinus
Output 7	Right Maxillary Sinus
Output 8	Right Sphenoid Sinus
Output 9	Left Septum
Output 10	Right Septum
Output 11	Left Main Nasal Cavity (MNC)
Output 12	Left Sphenoid Sinus
Output 13	Right Main Nasal Cavity (MNC)
Output 14	Left Frontal Sinus
Output 15	Left Ostiomeatal complex (OMC)
Output 16	Left Mid Turbinate
Output 17	Right Mid Turbinate
Output 18	Right Ostiomeatal complex (OMC)

Table 5.1: All 18 regions from all 10 anatomy geometries; each region is named output x to use as output from the machine learning tool.

$$RRSE = \sqrt{\frac{\sum_{i=1}^{n}(x_{i_{predicted}} - x_{i_{observed}})^2}{\sum_{i=1}^{n}(x_{i_{observed}} - \overline{x}_{observed})^2}} \tag{5.1}$$

Herein the term n in the above equation denotes the number of instances, where $x_{i_{predicted}}$ and $x_{i_{observed}}$ represent the actual and predicted values of regional deposition, respectively. $\overline{x}_{observed}$ represents the mean prediction value in the equation.

	Linear Regression		Random Forest		Multilayer Perceptron		Zero R	
	Correlation Coefficient	Root Relative Squared Error (%)	Correlation Coefficient	Root Relative Squared Error (%)	Correlation Coefficient	Root Relative Squared Error (%)	Correlation Coefficient	Root Relative Squared Error (%)
Output-1 Nasopharynx	0.1525	98.82%	0.7671	64.48%	0.3098	111.04%	-0.1883	100%
Output-2 Lower Airway	0.8689	49.39%	0.9589	28.38%	0.9388	35.53%	-0.1434	100%
Output-3 Left Ethmoid	0.2151	97.25%	0.4704	91.58%	0.3431	107.29%	-0.2177	100%
Output-4 Left Maxillary Sinus	0.0773	100.19%	0.3525	97.91%	0.0730	121.47%	-0.2214	100%
Output-5 Right Frontal Sinus	0.1367	98.51%	0.2001	105.26%	0.0765	99.86%	-0.2881	100%
Output-6 Right Ethmoid Sinus	0.3466	93.84%	0.5249	85.17%	0.2130	99.53%	-0.2186	100%
Output-7 Right Maxillary Sinus	0.0864	100.78%	0.4115	91.73%	0.2078	121.54%	-0.1979	100%
Output-8 Right Sphenoid Sinus	0.0077	102.02%	0.5216	87.30%	0.1101	51.62%	-0.2250	100%
Output-9 Left Septum	0.8616	50.63%	0.9556	29.42%	0.8656	63.91%	-0.1586	100%
Output-10 Right Septum	0.7411	66.97%	0.9395	34.34%	0.8023	101.28%	-0.1592	100%
Output-11 Left MNC	-0.0587	102.01%	0.9415	33.98%	0.3555	109.31%	-0.2780	100%
Output-12 Left Sphenoid	0.1683	98.33%	0.2505	104.68%	0.1477	97.47%	-0.3845	100%
Output-13 Right MNC	0.0492	100.62%	0.8745	48.52%	0.2987	91.65%	-0.2766	100%
Output-14 Left Frontal	0.4255	89.43%	0.5379	83.18%	0.5715	98.14%	-0.3754	100%
Output-15 Left OMC	0.4149	90.43%	0.5511	82.50%	0.5083	98.14%	-0.3733	100%
Output-16 Left Mid Turbinate	0.0842	101.19%	0.7189	69.31%	0.6390	81.97%	-0.2887	100%
Output-17 Right Mid Turbinate	0.0901	99.43%	0.5909	79.79%	0.3676	105.61%	0-.3184	100%
Output-18 Right OMC	0.0573	100.77%	0.6592	74.56%	0.1732	107.83%	-0.3487	100%

Table 5.2: The result of analysis (i) for 18 different outputs using 4 different algorithms i.e., linear regression, random forest, multilayer perceptron, zero R. For these statistical analyses the inputs for algorithms are: simulated pressure drops, volumetric flow rate, particle diameter, number of particles tracked, and output is deposition at the different region i.e., nasopharynx (output-1), lower airway (output-2).

5.2.4.1 ZeroR

ZeroR is a classifier in machine learning. It is a simple baseline classifier that always predicts the majority class in the training data. ZeroR does not take any input features or attributes into account and ignores any relationships between the input and output variables. While ZeroR is not useful for making accurate predictions on most datasets, it can be a useful baseline to compare against other more complex classification models. By comparing the performance of a more advanced classifier to the ZeroR classifier, we can get an idea of how much improvement the more advanced model provides over a simple baseline [86]. Here, the ZeroR classifier provides a baseline performance as a benchmark to compare to other classifiers by selecting the most frequent target (in this case particle deposition at a given region) value, ignoring all input parameters.

5.2.4.2 Multilayer Perceptron

A Multilayer Perceptron (MLP) Regressor is a type of neural network that is used for regression problems. It is a supervised learning algorithm that learns the relationship between a set of input features and a continuous output variable. In terms of n instances, an MLP

	Linear Regression		Random Forest		Multilayer Perceptron		Zero R		Number of instances
	Correlation Coefficient	Root Relative Squared Error (%)	Correlation Coefficient	Root Relative Squared Error (%)	Correlation Coefficient	Root Relative Squared Error (%)	Correlation Coefficient	Root Relative Squared Error (%)	
Output-1 Nasopharynx	0.3017	96.99%	0.4700	90.83%	0.6724	91.36%	-0.1883	100%	160
Output-2 Lower Airway	0.8608	50.81%	0.9557	35.21%	0.9639	27.87%	-0.1434	100%	160
Output-3 Left Ethmoid	0.4978	86.66%	0.5472	76.72%	0.6291	189.36%	-0.2186	100%	144
Output-4 Left Maxillary Sinus	0.5492	83.23%	0.6387	76.72%	0.3276	146.32%	-0.2214	100%	144
Output-5 Right Frontal Sinus	0.3544	94.10%	0.2901	101.11%	0.1545	117.77%	-0.2881	100%	144
Output-6 Right Ethmoid Sinus	0.4395	95.65%	0.5364	85.07%	0.6923	83.29%	-0.2751	100%	144
Output-7 Right Maxillary Sinus	0.3123	95.09%	0.5411	84.48%	0.4672	112.87%	-0.1979	100%	144
Output-8 Right Sphenoid Sinus	0.3352	47.16%	0.5328	85.68%	0.4112	111.14%	-0.2250	100%	144
Output-9 Left Septum	0.8783	50.89%	0.9193	41.75%	0.9599	28.59%	-0.3676	100%	128
Output-10 Right Septum	0.8558	53.49%	0.9379	36.89%	0.9610	28.68%	-0.3979	100%	128
Output-11 Left MNC	0.8420	96.63%	0.9139	40.70%	0.9575	30.25%	-0.2780	100%	128
Output-12 Left Sphenoid	0.2723	68.04%	0.2890	100.64%	0.1377	133.08%	-0.3845	100%	128
Output-13 Right MNC	0.7311	85.07%	0.8462	53.33%	0.9207	40.15%	-0.2766	100%	128
Output-14 Left Frontal	0.5091	84.49%	0.5464	82.76%	0.6524	82.87%	-0.3754	100%	112
Output-15 Left OMC	0.5075	97.66%	0.4938	86.05%	0.7079	80.03%	-0.4960	100%	80
Output-16 Left Mid Turbinate	0.2512	100.67%	0.7416	67.57%	0.8660	49.72%	-0.4040	100%	80
Output-17 Right Mid Turbinate	0.0519	97.46%	0.6590	74.25%	0.5845	86.13%	-0.3598	100%	96
Output-18 Right OMC	0.2708	100.77%	0.5957	79.85%	0.5233	139.77%	-0.2451	100%	80

Table 5.3: The result of analysis (ii) for 18 different outputs using 4 different algorithms i.e., linear regression, random forest, multilayer perceptron, zero R. For these statistical analyses the inputs for algorithms are simulated pressure drops, volumetric flow rate, particle diameter, number of particles tracked, geometric features (left nostril circumference, right nostril circumference, coronal width, penetrative depth, left nostril height, right nostril height, outlet plane surface area, outlet plane circumference, total internal nasal cavity volume, the surface area of a specific region, volume for the specific region), and output is deposition at the different region i.e., nasopharynx (output-1), lower airway (output-2).

	Linear Regression		Random Forest		Multilayer Perceptron		Zero R		Number of Physical Components
	Correlation Coefficient	Root Relative Squared Error (%)	Correlation Coefficient	Root Relative Squared Error (%)	Correlation Coefficient	Root Relative Squared Error (%)	Correlation Coefficient	Root Relative Squared Error (%)	
Output-1 Nasopharynx	0.3404	94.83%	0.6150	78.78%	0.6885	86.18%	-0.1883	100%	6
Output-2 Lower Airway	0.8609	50.81%	0.9635	29.883%	0.955	30.00%	-0.1434	100%	6
Output-3 Left Ethmoid	0.4747	88.01%	0.5729	82.06%	0.8714	51.17%	-0.2177	100%	6
Output-4 Left Maxillary Sinus	0.5219	84.91%	0.6291	77.51%	0.5925	88.04%	-0.2186	100%	6
Output-5 Right Frontal Sinus	0.1908	99.38%	0.2738	103.51%	0.3220	111.93%	-0.2881	100%	5
Output-6 Right Ethmoid Sinus	0.4313	90.14%	0.5540	83.89%	0.6090	99.08%	-0.2751	100%	6
Output-7 Right Maxillary Sinus	0.2955	96.42%	0.5681	82.02%	0.5045	112.09%	-0.1979	100%	6
Output-8 Right Sphenoid Sinus	0.3408	95.41%	0.5252	86.66%	0.3943	110.85%	-0.2250	100%	6
Output-9 Left Septum	0.8737	47.98%	0.9429	34.55%	0.9570	30.02%	-0.3676	100%	5
Output-10 Right Septum	0.8425	53.02%	0.9582	30.15%	0.9512	31.65%	-0.3979	100%	5
Output-11 Left MNC	0.7811	62.03%	0.9255	37.83%	0.3930	35.18%	-0.2780	100%	5
Output-12 Left Sphenoid	0.1810	99.62%	0.2553	102.82%	0.1433	134.57%	-0.3845	100%	5
Output-13 Right MNC	0.8961	71.77%	0.8643	50.22%	0.8876	48.62%	-0.2766	100%	5
Output-14 Left Frontal	0.5419	82.93%	0.5398	83.14%	0.7126	71.13%	-0.3754	100%	5
Output-15 Left OMC	0.5340	82.55%	0.4981	86.42%	0.7556	74.32%	-0.4960	100%	4
Output-16 Left Mid Turbinate	0.1535	103.50%	0.6920	71.74%	0.8516	54.03%	-0.4040	100%	3
Output-17 Right Mid Turbinate	0.2216	97.63%	0.6539	74.75%	0.8087	64.74%	-0.3598	100%	4
Output-18 Right OMC	0.2334	99.24%	0.6230	77.87%	0.3562	138.52%	-0.2451	100%	3

Table 5.4: The result of analysis (iii) for 18 different outputs using 4 different algorithms i.e., linear regression, random forest, multilayer perceptron, zero R. For these statistical analyses the inputs for algorithms are: simulated pressure drops, volumetric flow rate, particle diameter, physical components (PC_1, PC_2, PC_3, PC_4, PC_5(if available), PC_6 (if available), and output is deposition at the different region i.e., nasopharynx (output-1), lower airway (output-2).

Regressor can be trained on a dataset consisting of n instances, where each instance has m input features and a corresponding output value. During training, the MLP Regressor learns to map the input features to the output value using a set of weights and biases. The MLP Regressor consists of multiple layers of neurons, where each neuron applies a nonlinear activation function to the weighted sum of its inputs. The output of one layer serves as the input to the next layer, and the final output of the MLP Regressor is the predicted output value for a given set of input features [85]. In a neural network, every node produces a local output and transmits it to the subsequent layer of nodes in a deeper hidden layer until it reaches the output nodes in the output layer. The standard operation for computing the predicted output for a dataset of n groups of records by the i^{th} neuron is depicted in Equation 5.2.

$$O_i = f\left(\sum_{m=1}^{n} I_m W_{mi} + b_i\right) \tag{5.2}$$

Here I symbolizes the input, b denotes the bias of the node, W is the weighting factor, and f signifies the activation function.

5.2.4.3 Linear Regression

Linear Regression is a statistical approach to establishing the relationship between a dependent variable and one or more independent variables. It is a commonly used method in data analysis and machine learning for predicting future outcomes based on past data. The goal of linear regression is to find the best-fit line that minimizes the difference between the actual and predicted values of the dependent variable [87].

$$y = mx + b \tag{5.3}$$

Herein y is the dependent variable, x is the independent variable, m is the slope, and b is the intercept.

5.2.4.4 Random Forest

Random Forest is an ensemble learning method that combines multiple decision trees to produce a more accurate and robust model. The algorithm works by creating a set of decision trees based on different subsets of the training data and features. Each decision tree in the forest is trained on a random subset of the data and a random subset of the features. During training, each tree makes a decision based on its features and values, and the decision is based on the majority vote of the trees in the forest and the equation used to find out the correlation coefficient by using random forest [88] is here,

$$r = \frac{(n\Sigma xy - \Sigma x\Sigma y)}{\sqrt{(n\Sigma x^2 - \Sigma x^2)(n\Sigma y^2 - \Sigma y^2)}} \tag{5.4}$$

where r is the correlation coefficient, n is the number of samples, Σxy is the sum of the product of the predicted and true values, Σx and Σy are the sum of the predicted and true values, respectively, and $\sum x^2$ and Σy^2 is the sum of the squared predicted and true values, respectively.

5.3 Results

5.3.1 Prediction of drug delivery at the respirator regions

The results obtained from the analysis (i) of predictive models are presented in Table 5.2. Upon analyzing the correlation coefficient and root relative square error, it is evident that the predicted values for regional deposition were not accurate for analysis (i). Similarly, the results were also unsatisfactory for analyses (ii) and (iii) to predict regional depositions, as indicated by Tables 5.3, 5.4.

However, it was observed that the predictive accuracy for certain regions was better than others. Specifically, the regions of the lower airway, left septum, right septum, left main

	Random Forest			Multilayer Perceptron		
	Analysis (i) Correlation/Root Relative Squared Error	Analysis (ii) Correlation/Root Relative Squared Error	Analysis (iii) Correlation/Root Relative Squared Error	Analysis (i) Correlation/Root Relative Squared Error	Analysis (ii) Correlation/Root Relative Squared Error	Analysis (iii) Correlation/Root Relative Squared Error
Output-2 Lower Airway	0.9589/28.38%	0.9557/35.21%	0.9635/29.88%	0.9388/35.53%	0.9639/27.87%	0.9550/30.00%
Output-9 Left Septum	0.9556/29.42%	0.9193/41.75%	0.9429/34.55%	0.8656/63.91%	0.9599/28.59%	0.957/30.02%
Output-10 Right Septum	0.9395/34.34%	0.9379/36.89%	0.9582/30.15%	0.8023/101.28%	0.9610/28.67%	0.9512/31.65%
Output-11 Left MNC	0.9415/33.98%	0.9139/40.70%	0.9255/37.83%	0.3555/109.31%	0.0.9575/30.25%	0.393/35.18%
Output-13 Right MNC	0.8745/48.52%	0.8462/53.33%	0.8643/50.22%	0.2987/91.65%	0.9207/40.15%	0.7126/71.13%

Table 5.5: The better regional predictions of deposition using random forest and multilayer perception algorithms.

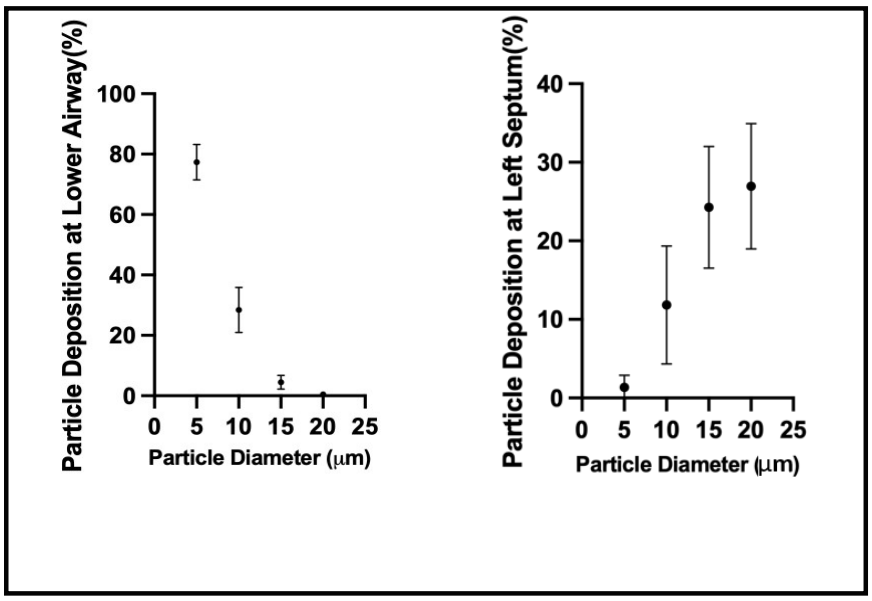

Figure 5.2: Represents the relation of particle deposition at lower airway and left septum with the particle diameter

nasal cavity (MNC), and right main nasal cavity (MNC) demonstrated higher predictive accuracy, as depicted in Fig 5.5. Furthermore, the use of random forest and multilayer perceptron algorithms proved to be the most effective in predicting the deposition of particles in these regions.

5.3.2 Correlations with particle diameter

The results presented in Fig 5.2 demonstrate that smaller particles have a higher deposition rate in the lower airway compared to larger particles. This is attributed to the lower inertia of smaller particles, which allows them to easily navigate through the flow and penetrate deeper into the lower airway. Conversely, larger particles exhibit a higher deposition rate at

the airway wall due to their greater diameter, which causes them to collide more frequently with the airway surface. These findings provide insight into the behavior of particles in the respiratory system and can inform the development of more effective inhalation therapies.

Chapter 6

Influence of pig nasal morphology on airflow, thermal regulation and tracking particle capture trends in bio-inspired channels

6.1 Overview

The nose is an essential component for mammalian survival because it regulates the temperature and humidity of breathed air before it enters the internal body. Unfortunately, little is known about the morphological characteristics of the nose and their influence on airflow patterns, heat transfer dynamics, and particulate capture. Hence, we undertook collaborative research in our lab to investigate the fundamental characteristics of the nasal cavity, such as tortuosity, the radius of curvature, and gap thickness, as well as their relationships with body weight. Our findings indicate that tortuosity has a crucial role in particle capture efficiency, especially in high-olfactory mammalian species such as pigs and opossums. By getting a greater comprehension of the fluid-particle interactions in nasal cavities, we can develop nature-inspired designs for a variety of engineering processes, such as the creation of new devices and filters. Consequently, it is essential to continue investigating the significance of heat management and particle screening in nasal structures in order to reveal

their mechanistic functions and translate this information into practical applications. Our collaborator at Cornell University developed the 3D pig model rebuilt from CT scan pictures, and in our lab, we did the logistics for inhaled airflow and heat transfer simulation in a truncated pig upper way.

This work was published in 2022 in Integrative and Comparative Biology under the title "Morphology of pig nasal structure and modulation of airflow and basic thermal conditioning".

6.2 Methods

Turbinates induce a series of flow patterns that contribute to the performance of various functions, including odorant and particle capture and thermal conditioning. We have elaborated on the morphological details of a representative pig nasal pathway through analysis of CT imaging data. The various methods used are indicated as follows.

6.2.1 CT scanning

We used a Toshiba Aquilion 16-slice CT scanner with a 0.5-mm slice thickness resolution and 512 pixels $\times$ 512 pixels in-plane resolution for a detailed view of the scanned nasal cavity of an averaged adult pig, as illustrated in figure 6.1(a). The pig's head was placed on a platform with the nose facing down. Then, CT scanning was done normal to the platform, which produced cross-sectional images perpendicular to the skin between the nostril and forehead. These CT-scan data provide a valuable basis for characterizing nasal airway structures and generating realistic computational models. Figure 6.1(b) shows a series of CT images of the pig nasal cavity mapped on the frontal plane at 2.4, 3.6, 7.3, 8.5, 10.9, and 14.6 cm from the nostril. Using a customized image processing and a photo editor, we have set the black region as representing an empty air passage and the white region representing the mixed bone, muscle, tissue, and blood inside the nose, as described

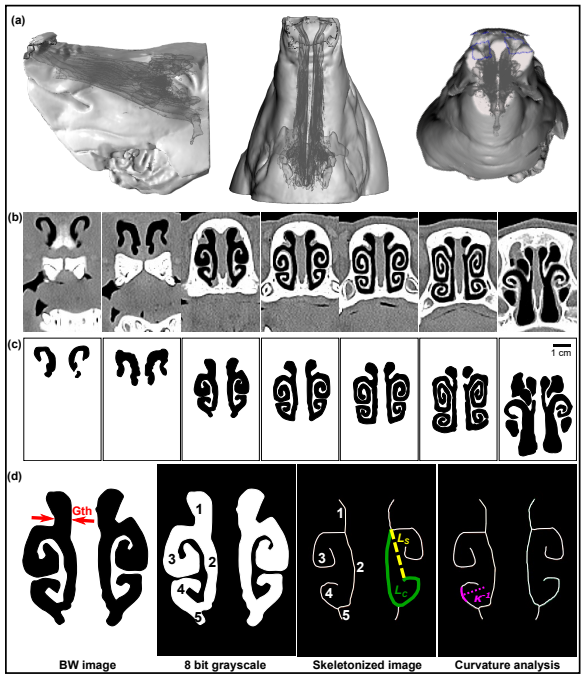

Figure 6.1: (a) A 3D pig model reconstructed from CT scan images of the front, top, and side views from left to right. The dark gray structure in the 3D model shows the nasal conduit. (b) Cross-sectional images of the pig's nasal cavity. Black regions denote cavities. Airway cross-section images from close-to-the-nostril to the nasopharynx are shown from left to right. (c) Images extracted from only the cavity part in (b). (d) Process for specifying the nose structure. Gap thickness is measured from black and white images extracted from CT scan images. Then, the color is inverted and converted to an 8-bit grayscale image, which is skeletonized, allowing determining distance, L_C, and displacement length, L_S, of each branch and curvature.
Courtesy: CT scanning of the animals airways was done by Dr. Sunghwan Jung's research group at the Department of Biological and Environmental Engineering at Cornell University.

in figure 6.1(c).

6.2.2 Gap thickness measurements

We explored the features of different animal species to put the analysis of the pig nose in perspective to comparable airway geometries. Images from different species were collected from various sources; in particular, CT scan images, magnetic resonance images, and anatomical images were obtained from selected resources [89, 90, 91, 92]. CT data for *Caluromys philander* (Bare-tailed woolly opossum), *Dasyurus hallucatus* (Northern quoll), *Potorous tridactylus* (Long-nosed potoroo), and *Petauroides volans* (Greater glider) were obtained from Dr. Macrini [89]. A female Labrador retriever's high-resolution magnetic resonance imaging (MRI) was acquired from Craven et al. [90], a male human MRI image was acquired from Shi at al. [93], a Rabbit's histological section image in dorsal view was

obtained from Casteleyn et al. [91], and *Cavia porcellus* (Guinea pig)'s CT scan images aquired from Rodgers [92, 93]. These cross-sectional images are located in the middle of the entire nasal cavity of each animal and contain the maxilloturbinal structure. However, depending on the animal's nasal characteristics, a portion of the olfactory region of the nasal cavity could be included in the nasal images.

The analysis of the noses first considers the size of the passage in the nasal cavity. Here, we define the gap thickness as the width of the air passageway, not its length. The images were treated using ImageJ™ and calibrated with a line tool. The thickness was measured manually by the side length of the air passage, that is, the width of the channel. The gap thickness was measured at a minimum of 15 different locations, including the thickest and thinnest parts of the air passage.

6.2.3 Tortuosity measurements

Skeletonized images were used to determine tortuosity. The skeletonization process involves converting images to 8-bit grayscale images, which are processed with the ImageJ software, see figure 6.1 (d) – to determine the shortest distance, L_{S}, and the actual distance, L_{C}. In this case, the length measurements were estimated for all segments with two end-points, one junction, and one end-point, or more than one junction. Using this information, tortuosity was calculated by dividing the actual distance (L_{C}) by the shortest distance (L_{S}), accordingly the tortuosity, $\tau = L_{\mathrm{C}}/L_{\mathrm{S}}$.

6.2.4 Curvature measurements

Skeletonized images were used to determine the curvature, κ. We manually drew the lines along every branch and approximated curves using various points. This was used to estimate the average value and standard deviation of κ for each line.

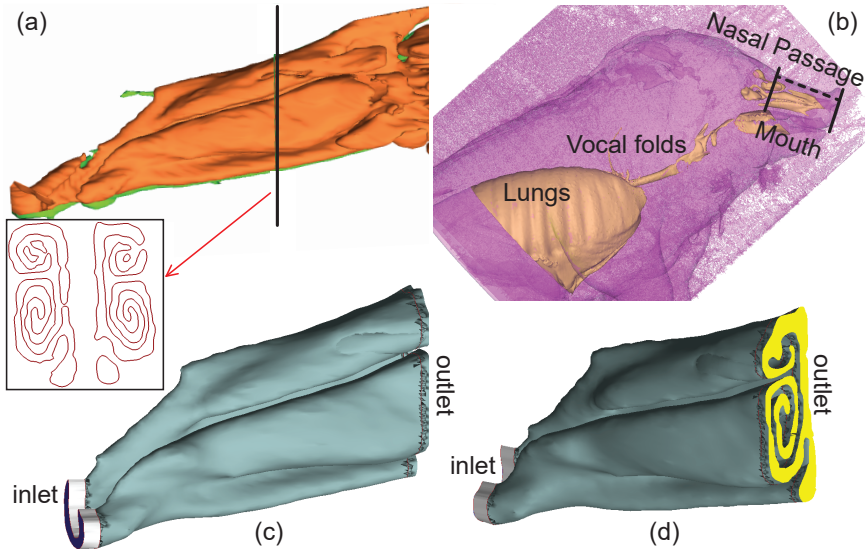

Figure 6.2: (a) CT-derived digital reconstruction of the nasal airway of a pig. The cross-sectional view depicts the turbinate structures on a representative section. (b) Reconstruction of a pig airway along the outline of the pig body. The segment bounded by the solid dark lines (and mapped via a dashed line) corresponds to the position of the panel (a) reconstruction. (c), (d) depict two separate views of the segmented model.

6.2.5 Numerical simulations of transport in the animal airway and bio-inspired cavities

We performed two series of numerical simulations on a finite volume solver; one focused on replicating realistic inhaled air flux and the associated heat transfer trends across the intra-airway tissues in a realistic CT-derived pig nasal cavity (see figure 6.2), and the other explored basic particle management phenomena in idealized conduits with different tortuosity, τ = 1.19 and 1.90 (see figure 6.5a). The τ = 1.90 case resembles typical tortuosities observable in the pig airway (see figure 6.4b). In contrast, the conduit with simpler geometric complexity, τ = 1.19, allowed examining the impact of tortuosity in particle management and capture of a phenomenon that has been postulated to elevate particle capturing along the upper respiratory airway, which also includes the olfactory epithelial region, in different mammalian species.

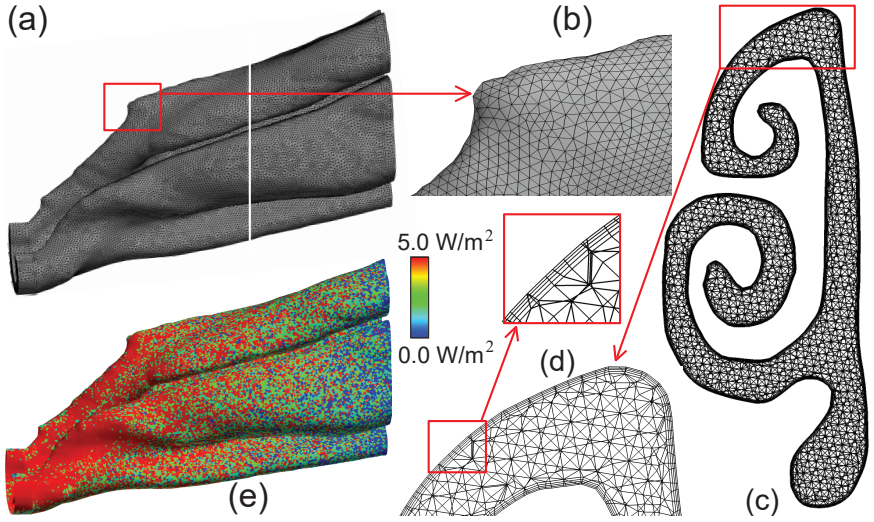

Figure 6.3: (a) Meshed model of the left nasal airway from the pig reconstruction in figure 6.2. (b) A zoomed-in visual of the exterior mesh profile. (c) Cross-section, along with zoomed-in visuals in (d) for the tetrahedral elements and the four prism layers extruded at the airway-tissue boundaries. (e) Heat flux map on the tissue surface for a simulated inhaled airflow of 40 L min^{-1}. The simulated data for heat transfer was post-processed and visualized on FieldView^{TM}, under license provided by Intelligent Light (Rutherford, NJ) through its University Partners Program.

6.2.6 Logistics for inhaled airflow and heat transfer simulation in a truncated pig upper airway

Large Eddy Simulations (LES) were performed in the digitized pig model (figure 6.2). The geometry was rebuilt from scans imaged at 0.5 mm depth increments. The geometry contains 1.1 million unstructured, graded tetrahedral elements and four prism layers of 0.1 mm thickness extruded at the air-tissue boundary, with a height ratio of 1. The simulations used a pressure-based transient solver with Kinetic Energy Transport Model (KETM) [45, 94] as the subgrid-scale model; it was implemented for a total of 1250 time-steps, with time-steps of 4×10^{-4} s. As a biophysical variable, heat flux correlates with the subjective sensation of nasal patency. The test simulations in the pig model imposed a thermal boundary condition of 20°C at the inlet and 32.6°C along the internal tissue walls [95, 96]; see figure 6.3. In addition, note that the simulated airflow rate was 40.0 L min^{-1}, under an imposed inlet-to-outlet pressure gradient of 2.90 Pa in the truncated airway model (figure 6.2). Therein, the numeric scheme considered the inlet entry near the nostrils to be a pressure-inlet, the posterior outlet was treated as a pressure-outlet, and the enclosing intra-nasal tissues are

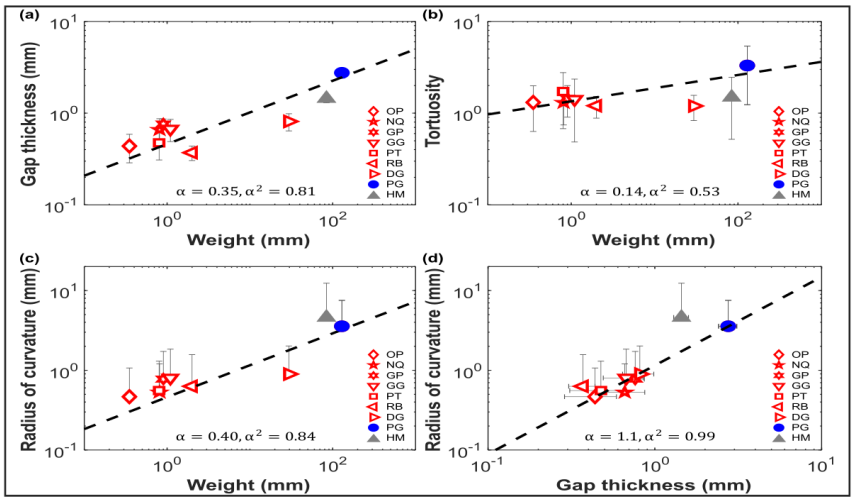

Figure 6.4: Basic relationship between animal weight and a) gap thickness, b) tortuosity, and c) radius of curvature. Dashed lines represent the trends for the animals, not including humans. (d) shows the relation of a radius of curvature versus gap thickness. The abbreviations Denote Opossum (OP), Northern Quoll (NQ), Guinea Pig (GP), Great Glider (GG), Potoroo (PT), Rabbit (RB), Dog (DG), Pig (PG), and Human (HM).

considered as rigid walls with no-slip boundary condition. The characteristic values for the ambient airflow included a density of 1.204 kg m^{-3}, dynamic viscosity of 1.825×10^{-5} kg m^{-1} s^{-1}, thermal conductivity of 0.0268 W m^{-1} K^{-1}, and specific heat of 1005.9 J kg^{-1} K^{-1} [97].

6.2.7 Logistics for tracking particle capture trends in bio-inspired channels

The simplified, bio-inspired tortuous channel geometries, with τ = 1.19 (figure 6.5a) and τ = 1.90 (figure 6.5b) contain 1.87 million and 1.40 million unstructured, graded tetrahedral elements, with four prism layers of 0.1 mm thickness at the airway walls with a height ratio of 1. The computational scheme operated on a segregated solver with SIMPLEC pressure-velocity coupling and second-order upwind spatial discretization. Pressure-driven flows of 15 L/min and 30 L/min were examined considering a section containing 312 channels defining an equivalent filter [4]. Each computation ran for 6 – 7 hours to complete a 0.35 s interval of simulated flow interval, with a time-step of 2×10^{-4} s. We consider an air density of 1.204 kg m^{-3} and the dynamic viscosity of air was set at 1.825×10^{-5} kg m^{-1} s^{-1}. The simulations enforced the following boundary conditions: (1) zero velocity at the airway

tissue interface, along with "trap" boundary condition for droplets, whereby the tracking of a droplet's transport would cease once it reaches the mesh layer lining the cavity walls; (2) zero pressure at inlets, which were the pressure-inlet zones in the simulations, with "reflect" boundary condition; and (3) a negative pressure at the outlet plane, which was the pressure-outlet zone, with "escape" boundary condition for the tracked particles, i.e., allowing for the outgoing particle to leave the test domain. To drive the 15 L/min air flux, the average inlet-to-outlet pressure gradient was -11.35 Pa, and at 30 L/min, the value was -35.12 Pa. The particle trajectories were tracked by Lagrangian-based discrete phase inert particle transport simulations against the ambient airflow, and additionally, the numerical scheme considered the effects of gravity and other body forces such as the Safman lift force exerted by a flow-shear field on small particulates moving transverse to the streamwise direction. In addition, a droplet size range with diameters $1 - 14$ μm was considered large enough to neglect the effects of Brownian motion. For the numerical tracking, the initial mass flow rate of the inert droplets moving normal to the inlet planes into the nasal airspace was required to be non-zero, and was set at 10^{-20} kg s^{-1}. The total number of monodispersed particles tracked for each tested size was 1338 in the τ = 1.19 conduit and 1076 in the τ = 1.90 conduit. Finally, the particle density was assumed to be 1.3 g/ml, commensurate with the physical properties for environmentally dehydrated, often pathogenic, particulates [1, 63].

6.3 Results

6.3.1 On the animal nasal structures

The air passage in the selected cross-sectional views was evaluated based on the nasal structure's width, tortuosity and curvature. The gray translucent internal part of the 3D views of a pig head, illustrated Figure 6.1(a), highlights the nasal structure.

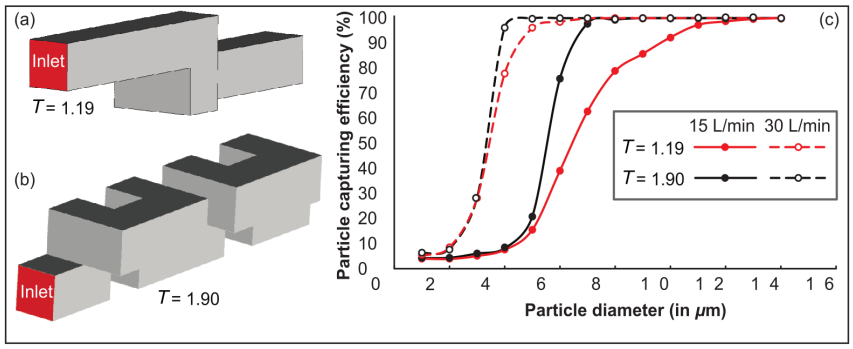

Figure 6.5: Idealized conduits with tortuosity τ = (a) 1.19 and (b) 1.90. c) Particle capturing trends for airflow rates of 15 L/min and 30 L/min through each pathway, averaged on an array of 312 inlet entries [4]. The red and black curves represent the 1.19 and 1.90 tortuosity cases. The trend lines during flow rates of 15 L/min and 30 L/min are shown by solid and dashed lines.

Figure 6.1(b) shows geometric changes along the nasal cavity from the nostril to the nasopharynx. Figure 6.1(c) illustrates these images in black and white binary coloring to explore the nasal cavity in detail. Here, the black region represents the nasal cavity. The first panel shows two nostrils and the second panel evidences slightly wider nostrils. Up to the second panel, both the right and left nostrils consist of air passages with a simple shape. However, a junction that divides an air passage into two or more paths is formed starting in the third image. From the third panel, the air passage is twisted in a spiral-like shape; this feature gradually enlarges and curls deeper in the nose, as indicated in the fourth, fifth, and sixth panels. As a consequence, the area of the nasal cavity increases. Figure 6.1(d) illustrates an example of the skeletonization steps that we used for the analysis. The binary images prepared for skeletonization allowed measuring the gap thickness. The channel passage size of the BW image in figure 6.1(d), D, can also be obtained with the cross-sectional area, A_c, and the perimeter, P, as $D = 4A_c/P$ [98], which gives a value of 6.2 mm. The variation of this quantity within the cross section is worth noting, which has a 3.6 mm average value.

The curvature and tortuosity were characterized based on the shape of the segments. As shown in figure 6.1(d), segment 1 is a thicker air pathway connected to the nostril, and connects to segments 2 and 3. Likewise, segment 2 connects to segments 4 and 5. Note that segments 3 and 4 have a spiral shape, whose tortuosity is 4.4 and 2.2, respectively.

However, segments 1, 2, and 5 are weakly curved. As a result, the associated tortuosity resulted in 1.1, 1.2, and 1.1. The radius of curvature in segments 3 and 4 is approximately 3.9 mm and 4.5 mm; it was 9.7, 6.4, 14.2 mm for segments of 1, 2, and 5. These quantities, namely, curvature and tortuosity, significantly varied along with the nose.

This process is repeated for the other animals; then, the tortuosity, gap thickness, and radius of curvature are linked to the animals' typical body weights to explore basic allometric relations. The body weight, W, was either the average value of the same species [99, 100, 101, 102, 103, 104, 105] or reported values [90, 91]. The various relationships are shown in Figure 6.4(a-c); they exhibit sub-quadratic power-law trends of the form $\psi \propto CW^{\alpha}$, where ψ represents the tortuosity, gap thickness, and radius of curvature, power α is illustrated in figure 6.4, and C is a characteristic constant. Relatively high $R^2 > 0.8$ of the radius of curvature and gap thickness evidence a clear dependence with bodyweight. In contrast, an $R^2 \approx 0.5$ between tortuosity and W indicates a weaker linkage. Remarkably, gap thickness and radius of curvature exhibit a very strong relation of $R^2 \approx 0.99$ with a quasi-linear relation with $\alpha \approx 1.1$.

The relations associated with a representative human nasal cavity are included to aid insight. Interestingly, the human nasal cavity does not follow the trends of animals. This may indicate distinct stressors modulating the evolution of functionality needs indicated here.

6.3.2 On the heat management and particle screening

In support of the *ansatz* about the importance of anatomic contortions in air warm-up, the total surface heat flux at the entry, marked by the left-anterior grey segment in figure 6.2 (c,d) is 7.59 Watt m^{-2}, which decayed to 0.034 Watt m^{-2} along the posterior airway walls (see figure 6.3 e). The conditioning of the air, as it moves into the posterior parts of the animal's nasal passage, is also quantifiable from the surface heat transfer coefficients which

reduce from 0.431 Watt m^{-2} K^{-1} at the entry to 0.002 Watt m^{-2} averaged over the rest of the airway.

The numerical inspection of particle screening trends in the idealized, bio-inspired channel geometries with τ = 1.19 and 1.90 show lower capturing efficiency, as hypothesized; see figure 6.5. The capturing efficiency for the two geometries is the same for comparatively small particles, namely viz. $\lesssim$3 μm for 30 L/min ambient air flux through the entire filtration unit, the same threshold being $\lesssim$4 μm for the 15 L/min flux. We note a 100% capturing efficiency for particle sizes $\gtrsim$ 6 μm during the 30 L/min flux and $\gtrsim$ 14 μm during the 15 L/min for the τ = 1.19 channel. The same thresholds for the τ = 1.90 channel are $\gtrsim$ 4 μm and $\gtrsim$ 7 μm, respectively.

Chapter 7

Discussion and Summary

The present study in Chapter 2 sheds light on the modeling of intranasal drug delivery, with a special focus on the ”Improved Used” approach to enhance the efficacy of drugs at infectious sites. Despite the promising results, some limitations were observed in this study, which must be considered in the interpretation of the findings. The following section highlights the discussions of the study in Chapter 2 :

- *On the limitations of respiratory flow modeling* – Realistic modeling of mucociliary transport along the morphologically complex airway cavity constitutes a significant open question in the domain of respiratory transport mechanics [106, 107, 108]. In this study, state-of-the-art algorithms have been implemented to identify the droplet sizes that are efficient at *direct* nasopharyngeal delivery, under the impact of inhaled airflow when sprayed into the intranasal space. However, a big caveat lies in what happens to the larger droplets that happen to deposit along the anterior parts of the airway. Quantifying their mucus-driven downstream transport mechanics and correlating that with the therapeutic efficacy of the drug solutes when they reach the posterior clinical target sites poses a vital translational challenge, which needs to be addressed by the interdisciplinary scientific community in the future.

- *On caveats regarding the tested droplet size range* – The tested droplet diameter range was 1 – 24 μm. While extracting the droplet sizes that would correspond to at least 2% nasopharyngeal deposition from a cluster of 3000 monodispersed droplets of each size, three of the eight test cases (i.e., the IU protocol data for left and right nostril ad-

ministration in two subjects under two inhalation rates) led to 24 μm as the maximum limit of such sizes; see Figs. 2.4 and 2.5. While that may justifiably raise the question on what happens if we consider droplets that are sized bigger than 24 μm, the focus of this study has been to pin down a common droplet size range that would be generically robust to inhaled airflow conditions and user subjectivities. Consequently, the bigger droplets were not tracked which tend to deposit mostly anteriorly, owing to the inertia-dominated initial phase of their trajectories when injected out of the nozzle; see our earlier publication [2] for an extensive related discussion. Also, as a side-note to this, it is relevant to consider that administered droplets, under nebulized conditions in the same two test subjects and with comparable material density (1.3 g/mL), had resulted in an ideal size range of 2.5 – 19 μm (i.e., comfortably smaller than 24 μm) for at least 5% targeted nasopharyngeal deposition; see another of earlier publications [1] from our lab for details.

- *On caveats related to the droplet transport modeling* – The Lagrangian particle tracking scheme used to track the sprayed droplets is one-way momentum coupled with the continuous ambient airflow field. Additionally, the droplet transport model ignores evaporation effects on the droplet constituents and any post-deposition displacement guided by the surface-bound mucociliary flux. First, in reality, momentum transfer from the nasal spray droplets to the surrounding airflow may indeed affect droplet motion and influence the nasal deposition patterns [109]. However, the one-way coupling approach for regional deposition prediction, apart from being computationally inexpensive, has been validated experimentally through multiple studies, both by us [2] and others [110, 111, 112]. Secondly, the droplet evaporation effects, while important for tracking the slow drug delivery process inside the lower airway along the branched bronchial pathways, could be considered negligible for drug delivery to sites in the upper respiratory tract, such as the nasopharynx. The time scale for sprayed droplet transport for direct nasopharyngeal deposition is merely on the order

of $\mathcal{O}(10^{-1})$ sec. [32]. With the scale at least 2 – 3 orders smaller than the evaporation time scale for a small droplet [113, 114, 115], we argue that the inclusion of evaporative effects in the numerical scheme will have a trivial impact on the direct deposition predictions at the nasopharynx. Finally, the non-consideration of the airway surface liquid flux, which could have otherwise estimated the post-deposition droplet dynamics, is a key limitation and a long-standing challenge, given the complex non-Newtonian rheology of the mucosal stream [116]. We will address this caveat in our future studies – especially to answer specific relevant questions, such as: (a) how long does a drug droplet stay at the target site before being swept by the mucus? (b) is the time scale from (a) sufficiently long for pharmaceutically effective tissue-level penetration of the drug solutes? and (c) What is the therapeutic ramification of mucus-driven transport of anteriorly-deposited drug solutes to the downstream target regions?

- *On the constraints posed by the reconstructed in silico geometries* – The CT-based anatomically realistic reconstructions, while accurately replicating the topological convolutions implicit [117] in a real tortuous respiratory cavity, still comes with the caveat of containing structurally rigid airway walls. However, though the rigidity of the walls (intended to mimic the internal tissue surfaces and cartilages) is somewhat unrealistic, the time-scale of inhaled transport is on the scale of 10^{-1} s [32] and the idealization could be considered a mechanistically feasible assumption that is sufficient to extract the fundamental nuances underlying such physiologically complex transport processes.

Chapter 3 presents the experimental validation of the numerical simulations discussed in Chapter 2. Despite the valuable insights gained from the experiments, certain limitations were encountered during the validation process. These limitations have important implications for the interpretation of the results and suggest areas for future research.

- Firstly, the injector was used instead of spray bottles during the experiment. Using spray bottles required a large number of pumps (approximately 500) to achieve a measurable volume of liquid from the back end of subject 3 (See the section 3.1.1). However, this limitation can now be addressed with the new setup in our laboratory (See the section 3.3).

- Secondly, water (density of 1 gm/ml) was used as the injected liquid during the experiment, whereas the simulation assumed a density of 1.3 gm/ml. This discrepancy between the experimental and simulated conditions may have affected the accuracy of the results.

- Finally, during the numerical simulation, the anatomy was placed in an inclined forward position, while the subject was held upright during the experiment to maintain a downward gravity direction. This difference in positioning may have introduced variability in the results and should be taken into account in future research.

Chapter 4 discusses the numerical modeling of airborne respiratory infections, with a focus on lower airway onset.

- A study on smallpox was conducted using only one subject due to time constraints. However, there are three more subjects available in the lab, presenting an opportunity to continue the study with new subjects.

The subsequent discussions delve into lower airway onset –

- *Limitations of the study for lower airway onset* – The results should be interpreted as being preliminary, given that the numerical findings are based on simulated data from only two test subjects. However, it should be noted that there is a good agreement between the numerical predictions of aspiration frequency with earlier observational

findings, which lends to the validity of the underlying computational and mathematical framework. The size of the projected viral dose also speaks to the robustness of the conclusion – it is likely that virion flow from the nasopharynx to the lungs occurs in large excess of the minimum dose required to seed a lung infection for many individuals, thereby precipitating a brisk aggravation of the disease symptoms. Note that, from a clinical standpoint, the contribution of mucociliary activity, propelling a bolus toward the oropharynx from the nasopharynx has not been considered. However, while that would theoretically increase the bolus volume and the potential frequency of aspiration, it would also provide a protective mechanism after aspiration, as the bolus could be propelled up through a reflux mechanism at the trachea. Finally, the aspirated pharyngeal liquid volumes could be significantly variable depending on other disease processes, including gastroesophageal reflux disease (GERD), which is very common in the United States [118, 119].

- *Clinical ramifications* – The findings suggest a simple aspiration-based physiological mechanism for COVID-19 etiology following initial SARS-CoV-2 infection in the nasopharynx. Such a mechanistic link may be valuable in identifying risk factors that predispose patients to progress to acute COVID-19 morbidity following SARS-CoV-2 infection. For example, a prediction that emerges readily from this proposed mechanism is that individuals with dysphagia (problems initiating swallowing) may be at increased risk of developing COVID-19 following SARS-CoV-2 onset, and may have more negative outcomes with the disease.

  One condition associated with dysphagia is obstructive sleep apnea (OSA) [120, 121, 122], with increased nocturnal aspiration [76] and risk of aspiration pneumonia [123]. Based on the mechanism proposed by us for viral spread to the lungs, individuals with OSA would thus be expected to be at a higher risk for COVID-19. In fact, this has been reported by a number of different investigators [124, 125, 126, 127, 128]. One study, for example, reported an association of OSA with increased risk

for hospitalization (OR 1.65; 95% CI (1.36, 2.02)) and respiratory failure (OR 1.98; 95% CI (1.65, 2.37)) owing to COVID-19, after adjusting for diabetes, hypertension, and body mass index [129]. As a practical matter, this work suggests that individuals with OSA should not suspend the use of their CPAP (continuous positive airway pressure) devices upon testing positive for SARS-CoV-2, as has been suggested by some practitioners [130].

Chapter 5 of the thesis focuses on the implementation of machine learning as a cost-effective method to forecast the deposition of inhaled particles along the human respiratory airspace based on anatomical geometric features. The subsequent discussions pertain to the outcomes of this study, including the following observations:

- The machine learning algorithm did not provide accurate predictions for all the regions of the respiratory airspace. This could be attributed to the inadequate amount of data used in the study. Although 160 data points were employed, this may not have been sufficient to produce reliable results using the machine learning approach. Furthermore, the use of a built-in function method might have contributed to the suboptimal results. The development of user-defined algorithms could help improve the accuracy of particle deposition predictions for all regions.

- The smaller diameter particles were observed to travel further through the nasal cavity than larger diameter particles. This can be explained by the lower inertia of smaller particles in comparison to their larger counterparts.

In Chapter 6, the process of thermal transmission in a pig's nasal cavity is examined. Following are discussions on this study:

- Regarding the geometric idealization and truncation of the anatomic airspaces, it should be pointed out that the CT-derived geometric model for the pig airway (e.g.,

see figures 6.2 and 6.3) is a truncated representation of its upper respiratory airspace. The demarcated cavity, however, does include part of the olfactory epithelial region [131] to ensure the relevance of the isolated anatomic geometry in context to olfactory mechanisms and the transport features involved therein. Nonetheless, it should be noted that the olfactory bulb is located further back in the nose [132], well past the truncated airway domain identified in panels c and d of figure 6.2. The pig upper respiratory space in our work comprises two main flow pathways in the main nasal cavity, namely the dorsal and ventral pathways. Part of the olfactory epithelium extends along the very upper recesses of the dorsal passage [131, 132, 133]. In addition, it should also be noted that excluding the posterior parts of the upper airway (going into the pharyngeal tract) in our test geometry – does not bear any appreciable effect on the flow physics tracked along the anterior airspace.

- In the numerical tests, the length scale of the tracked particles is on the order of microns (figure 6.5c), which is typical [134]. However, odorants that eventually stimulate the perception of smell are at molecular scale [135]; our modeling approach considers that tiny particles enter the animal nose in the larger droplets and aerosols. Our focus was on exploring the trapping characteristics, such as a pig's upper respiratory pathway owing to the complex airflow features affected by the incoming streamlines inside the topologically evolved and highly tortuous conduit.

The "Intellectual Merits" of this thesis are significant in that it addresses important questions related to respiratory infections, particularly in the context of COVID-19. The thesis investigates the fluid mechanics of the transmission of SARS-CoV-2 from the nasopharynx to the lower airway and quantifies the rate of virion transmission. The thesis also aims to optimize drug delivery through the nasal route and verify the efficacy of this approach through experimentation. Additionally, the thesis aims to construct a computational model capable of forecasting hazardous droplet size and infectious dosage for respiratory diseases

that spread through airborne transmission. The use of machine learning to predict regional deposition along the human respiratory airspace using geometric features of anatomies and the investigation of thermal characteristics present within the nasal cavity are also innovative contributions.

The “Broader Impacts” of this thesis are significant in that the findings can potentially inform the development of more effective drug delivery methods and treatments for respiratory infections, particularly COVID-19. The use of machine learning as a new tool to predict regional deposition along the human respiratory could reduce the operating costs of numerical simulation and enable faster and more accurate predictions of regional deposition. Additionally, the investigation of thermal transport processes in a pig’s nose can have broader implications for the understanding of animal adaptation to environmental situations. The thesis also highlights the importance of interdisciplinary research, particularly the integration of thermo-fluid physics and biological research, and can potentially inspire further interdisciplinary collaborations in these fields.

Bibliography

[1] S. Basu, "Computational characterization of inhaled droplet transport to the nasopharynx," *Scientific Reports*, vol. 11, pp. 1–13, 2021.

[2] S. Basu, L. T. Holbrook, K. Kudlaty, O. Fasanmade, J. Wu, A. Burke, B. W. Langworthy, Z. Farzal, M. Mamdani, W. D. Bennett, J. P. Fine, B. A. Senior, *et al.*, "Numerical evaluation of spray position for improved nasal drug delivery," *Scientific Reports*, vol. 10, no. 1, pp. 1–18, 2020.

[3] S. Basu, L. T. Holbrook, K. Kudlaty, O. Fasanmade, J. Wu, A. Burke, B. W. Langworthy, Z. Farzal, M. Mamdani, W. D. Bennett, *et al.*, "Numerical evaluation of spray position for improved nasal drug delivery," *Scientific reports*, vol. 10, no. 1, p. 10568, 2020.

[4] J. Yuk, A. Chakraborty, S. Cheng, C. I. Chung, A. Jorgensen, S. Basu, L. P. Chamorro, and S. Jung, "On the design of particle filters inspired by animal noses," *Journal of The Royal Society Interface*, vol. 19, no. 20210849, pp. 1–8, 2022.

[5] Johns-Hopkins-University, "Coronavirus Resource Center." Web link, accessed 3-April-2022.

[6] R. Mittal, R. Ni, and J. H. Seo, "The flow physics of COVID-19," *Journal of Fluid Mechanics*, vol. 894, 2020.

[7] Y. J. Hou, K. Okuda, C. E. Edwards, D. R. Martinez, T. Asakura, K. H. Dinnon III, T. Kato, R. E. Lee, B. L. Yount, T. M. Mascenik, *et al.*, "SARS-CoV-2 Reverse Genetics Reveals a Variable Infection Gradient in the Respiratory Tract," *Cell*, 2020.

[8] N. J. Matheson and P. J. Lehner, "How does SARS-CoV-2 cause COVID-19?," *Science*, vol. 369, no. 6503, pp. 510–511, 2020.

[9] M. E. Ortiz, A. Thurman, A. A. Pezzulo, M. R. Leidinger, J. A. Klesney-Tait, P. H. Karp, P. Tan, C. Wohlford-Lenane, P. B. McCray Jr, and D. K. Meyerholz, "Heterogeneous expression of the SARS-Coronavirus-2 receptor ACE2 in the human respiratory tract," *EBioMedicine*, vol. 60, p. 102976, 2020.

[10] M. R. Patel, D. Carroll, E. Ussery, H. Whitham, C. A. Elkins, J. Noble-Wang, J. K. Rasheed, X. Lu, S. Lindstrom, V. Bowen, *et al.*, "Performance of oropharyngeal swab testing compared to nasopharyngeal swab testing for diagnosis of COVID-19," *Clinical Infectious Diseases*, 2020.

[11] K. Gleeson, S. L. Maxwell, and D. F. Eggli, "Quantitative aspiration during sleep in normal subjects," *Chest*, vol. 111, no. 5, pp. 1266–1272, 1997.

[12] S. G. Butler, A. Stuart, X. Leng, C. Rees, J. Williamson, and S. B. Kritchevsky, "Factors influencing aspiration during swallowing in healthy older adults," *The Laryngoscope*, vol. 120, no. 11, pp. 2147–2152, 2010.

[13] R. Wölfel, V. M. Corman, W. Guggemos, M. Seilmaier, S. Zange, M. A. Müller, D. Niemeyer, T. C. Jones, P. Vollmar, C. Rothe, *et al.*, "Virological assessment of hospitalized patients with COVID-2019," *Nature*, vol. 581, no. 7809, pp. 465–469, 2020.

[14] D. Van Egeren, A. Novokhodko, M. Stoddard, U. Tran, B. Zetter, M. Rogers, B. L. Pentelute, J. M. Carlson, M. Hixon, D. Joseph-McCarthy, and A. Chakravarty, "Risk of rapid evolutionary escape from biomedical interventions targeting SARS-CoV-2 spike protein," *PloS One*, vol. 16, no. 4, p. e0250780, 2021.

[15] M. Pachetti, B. Marini, F. Benedetti, F. Giudici, E. Mauro, P. Storici, C. Masciovecchio, S. Angeletti, M. Ciccozzi, R. C. Gallo, *et al.*, "Emerging SARS-CoV-2 mutation hot spots include a novel RNA-dependent-RNA polymerase variant," *Journal of Translational Medicine*, vol. 18, no. 1, pp. 1–9, 2020.

[16] A. Giri, N. Biswas, D. L. Chase, N. Xue, M. Abkarian, S. Mendez, S. Saha, and H. A. Stone, "Colliding respiratory jets as a mechanism of air exchange and pathogen transport during conversations," *Journal of Fluid Mechanics*, vol. 930, 2022.

[17] F. Yang, A. A. Pahlavan, S. Mendez, M. Abkarian, and H. A. Stone, "Towards improved social distancing guidelines: Space and time dependence of virus transmission from speech-driven aerosol transport between two individuals," *Physical Review Fluids*, vol. 5, no. 12, p. 122501, 2020.

[18] A. L. Valesano, K. E. Rumfelt, D. E. Dimcheff, C. N. Blair, W. J. Fitzsimmons, J. G. Petrie, E. T. Martin, and A. S. Lauring, "Temporal dynamics of SARS-CoV-2 mutation accumulation within and across infected hosts," *PLoS Pathogens*, vol. 17, no. 4, p. e1009499, 2021.

[19] Y. Wang, D. Wang, L. Zhang, W. Sun, Z. Zhang, W. Chen, A. Zhu, Y. Huang, F. Xiao, J. Yao, *et al.*, "Intra-host variation and evolutionary dynamics of SARS-CoV-2 populations in COVID-19 patients," *Genome Medicine*, vol. 13, no. 1, pp. 1–13, 2021.

[20] R. Schroter and N. Watkins, "Respiratory heat exchange in mammals," *Respiration physiology*, vol. 78, no. 3, pp. 357–367, 1989.

[21] M. Wolf, S. Naftali, R. C. Schroter, and D. Elad, "Air-conditioning characteristics of the human nose," *The Journal of Laryngology & Otology*, vol. 118, no. 2, pp. 87–92, 2004.

[22] D. Elad, S. Naftali, M. Rosenfeld, and M. Wolf, "Physical stresses at the air-wall interface of the human nasal cavity during breathing," *Journal of applied physiology*, vol. 100, no. 3, pp. 1003–1010, 2006.

[23] D. Doorly, D. Taylor, A. Gambaruto, R. Schroter, and N. Tolley, "Nasal architecture: form and flow," *Philosophical Transactions of the Royal Society A: Mathematical, Physical and Engineering Sciences*, vol. 366, no. 1879, pp. 3225–3246, 2008.

[24] R. B. Boyd, "A gross and microscopic study of the respiratory anatomy of the antarctic weddell seal, leptonychotes weddelli," *Journal of Morphology*, vol. 147, no. 3, pp. 309–335, 1975.

[25] J.-A. Mellish, A. Hindle, J. Skinner, and M. Horning, "Heat loss in air of an antarctic marine mammal, the weddell seal," *Journal of Comparative Physiology B*, vol. 185, pp. 143–152, 2015.

[26] G. J. M. Garcia, J. D. Schroeter, R. A. Segal, J. Stanek, G. L. Foureman, and J. S. Kimbell, "Dosimetry of nasal uptake of water-soluble and reactive gases: a first study of interhuman variability," *Inhalation Toxicology*, vol. 21, no. 7, pp. 607–618, 2009.

[27] X. He, T. Reponen, R. T. McKay, and S. A. Grinshpun, "Effect of particle size on the performance of an n95 filtering facepiece respirator and a surgical mask at various breathing conditions," *Aerosol Science and Technology*, vol. 47, no. 11, pp. 1180–1187, 2013.

[28] D. O. Frank-Ito, M. Wofford, J. D. Schroeter, and J. S. Kimbell, "Influence of mesh density on airflow and particle deposition in sinonasal airway modeling," *Journal of Aerosol Medicine and Pulmonary Drug Delivery*, vol. 29, no. 1, pp. 46–56, 2016.

[29] S. Basu, N. Witten, and J. S. Kimbell, "Influence of localized mesh refinement on numerical simulations of post-surgical sinonasal airflow," *Journal of Aerosol Medicine and Pulmonary Drug Delivery*, vol. 30, no. 3, pp. A–14, 2017.

[30] K. Inthavong, J. Ma, Y. Shang, J. Dong, A. S. R. Chetty, J. Tu, and D. O. Frank-Ito, "Geometry and airflow dynamics analysis in the nasal cavity during inhalation," *Clinical Biomechanics*, vol. 66, pp. 97–106, 2019.

[31] Y. Zhang, Y. Shang, K. Inthavong, Z. Tong, B. Sun, K. Zhu, A. Yu, and G. Zheng, "Computational investigation of dust mite allergens in a realistic human nasal cavity," *Inhalation Toxicology*, vol. 31, no. 6, pp. 224–235, 2019.

[32] S. Basu, D. O. Frank-Ito, and J. S. Kimbell, "On computational fluid dynamics models for sinonasal drug transport: Relevance of nozzle subtraction and nasal vestibular dilation," *International Journal for Numerical Methods in Biomedical Engineering*, vol. 34, no. 4, p. e2946, 2018.

[33] Z. Farzal, S. Basu, A. Burke, O. O. Fasanmade, E. M. Lopez, W. D. Bennett, C. S. Ebert Jr, A. M. Zanation, B. A. Senior, and J. S. Kimbell, "Comparative study of simulated nebulized and spray particle deposition in chronic rhinosinusitis patients," in *International Forum of Allergy & Rhinology*, vol. 9, pp. 746–758, Wiley Online Library, 2019.

[34] J. S. Kimbell, S. Basu, G. J. M. Garcia, D. O. Frank-Ito, F. Lazarow, E. Su, D. Protsenko, Z. Chen, J. S. Rhee, and B. J. Wong, "Upper airway reconstruction using long-range optical coherence tomography: Effects of airway curvature on airflow resistance," *Lasers in Surgery and Medicine*, vol. 51, no. 2, pp. 150–160, 2019.

[35] S. N. Brown and K. Stewartson, "Laminar separation," *Annual Review of Fluid Mechanics*, vol. 1, no. 1, pp. 45–72, 1969.

[36] F. T. Smith, "Steady and unsteady boundary-layer separation," *Annual Review of Fluid Mechanics*, vol. 18, no. 1, pp. 197–220, 1986.

[37] S. Basu and M. A. Stremler, "Exploring the dynamics of '2P' wakes with reflective symmetry using point vortices," *Journal of Fluid Mechanics*, vol. 831, pp. 72–100, 2017.

[38] S. Basu and M. A. Stremler, "On the motion of two point vortex pairs with glide-reflective symmetry in a periodic strip," *Physics of Fluids*, vol. 27, no. 10, p. 103603, 2015.

[39] M. A. Stremler and S. Basu, "On point vortex models of exotic bluff body wakes," *Fluid Dynamics Research*, vol. 46, no. 6, p. 061410, 2014.

[40] M. A. Stremler, S. Basu, and E. Masroor, "Streamline patterns in 2P vortex street equilibria – CORRIGENDUM," *Journal of Fluid Mechanics*, vol. 901, 2020.

[41] P. W. Longest and S. Vinchurkar, "Validating CFD predictions of respiratory aerosol deposition: effects of upstream transition and turbulence," *Journal of biomechanics*, vol. 40, no. 2, pp. 305–316, 2007.

[42] E. L. Perkins, S. Basu, G. J. M. Garcia, R. A. Buckmire, R. N. Shah, and J. S. Kimbell, "Ideal particle sizes for inhaled steroids targeting vocal granulomas: preliminary study using computational fluid dynamics," *Otolaryngology–Head and Neck Surgery*, vol. 158, no. 3, pp. 511–519, 2018.

[43] S. Hosseini, T. A. Schuman, R. Walenga, J. V. Wilkins Jr, A. Babiskin, and L. Golshahi, "Use of anatomically-accurate 3-dimensional nasal airway models of adult human subjects in a novel methodology to identify and evaluate the internal nasal valve," *Computers in Biology and Medicine*, p. 103896, 2020.

[44] D. J. Doorly, D. J. Taylor, and R. C. Schroter, "Mechanics of airflow in the human nasal airways," *Respiratory Physiology & Neurobiology*, vol. 163, no. 1-3, pp. 100–110, 2008.

[45] N. Baghernezhad and O. Abouali, "Different SGS models in Large Eddy Simulation of 90 degree square cross-section bends," *Journal of Turbulence*, no. 11, p. N50, 2010.

[46] M. Alfadhel, U. Puapermpoonsiri, S. J. Ford, F. J. McInnes, and C. F. van der Walle, "Lyophilized inserts for nasal administration harboring bacteriophage selective for Staphylococcus aureus: in vitro evaluation," *International Journal of Pharmaceutics*, vol. 416, no. 1, pp. 280–287, 2011.

[47] Y. Michael, M. J. Snowden, B. Z. Chowdhry, I. C. Ashurst, C. J. Davies-Cutting, and T. Riley, "Characterisation of the aggregation behaviour in a salmeterol and fluticasone propionate inhalation aerosol system," *International Journal of Pharmaceutics*, vol. 221, no. 1-2, pp. 165–174, 2001.

[48] A. Pharma, "Valos VP7 Spray Pump." White Paper link, accessed 18-January-2022.

[49] X. Liu, W. H. Doub, and C. Guo, "Assessment of the influence factors on nasal spray droplet velocity using phase-Doppler anemometry," *AAPS Pharmscitech*, vol. 12, no. 1, pp. 337–343, 2011.

[50] S. Basu, Z. Farzal, and J. S. Kimbell, ""Magical" fluid pathways: inspired airflow corridors for optimal drug delivery to human sinuses," in *APS Division of Fluid Dynamics Meeting Abstracts*, pp. L4–004, 2017.

[51] W. H. Finlay, *The Mechanics of Inhaled Pharmaceutical Aerosols: An Introduction*. Academic Press, 2001.

[52] M. S. Benninger, J. A. Hadley, J. D. Osguthorpe, B. F. Marple, D. A. Leopold, M. J. Derebery, and M. Hannley, "Techniques of intranasal steroid use," *Otolaryngology – Head and Neck Surgery*, vol. 130, no. 1, pp. 5–24, 2004.

[53] V. Kundoor and R. N. Dalby, "Effect of formulation-and administration-related variables on deposition pattern of nasal spray pumps evaluated using a nasal cast," *Pharmaceutical Research*, vol. 28, no. 8, pp. 1895–1904, 2011.

[54] "Fluticasone propionate nasal spray instructions." http://dailymed.nlm.nih.gov/dailymed/archives/fdaDrugInfo.cfm?archiveid=5767. accessed 21-September-2013.

[55] Flonase, "How to Properly Use Nasal Spray for Allergy Relief." White Paper link, accessed 11-February-2022.

[56] J. S. Kimbell, S. Basu, Z. Farzal, and B. A. Senior, "Characterizing nasal delivery in 3D models before and after sinus surgery," *Respiratory Drug Delivery*, vol. 1, pp. 181–188, 2018.

[57] S. Treat, C. S. Ebert Jr, Z. Farzal, S. Basu, A. M. Zanation, B. D. Thorp, J. S. Kimbell, B. A. Senior, and A. J. Kimple, "Intranasal corticosteroids: patient administration angles and impact of education," *Rhinology Online*, 2020.

[58] S. Balachandar, "A scaling analysis for point–particle approaches to turbulent multiphase flows," *International Journal of Multiphase Flow*, vol. 35, no. 9, pp. 801–810, 2009.

[59] DailyMed, "Us national library of medicine: Fluticasone propionate spray – drug label information." Link, 2023.

[60] Drugs.com, "Nasacort dosage." Link, 2023.

[61] Y. S. Cheng, T. D. Holmes, J. Gao, R. A. Guilmette, S. Li, Y. Surakitbanharn, and C. Rowlings, "Characterization of nasal spray pumps and deposition pattern in a replica of the human nasal airway," *Journal of Aerosol Medicine*, vol. 14, no. 2, pp. 267–280, 2001.

[62] S. Basu, "Computational characterization of inhaled droplet transport to the nasopharynx," *Scientific Reports*, vol. 11, no. 1, p. 6652, 2021.

[63] V. Stadnytskyi, C. E. Bax, A. Bax, and P. Anfinrud, "The airborne lifetime of small speech droplets and their potential importance in SARS-CoV-2 transmission," *Proceedings of the National Academy of Sciences*, vol. 117, no. 22, pp. 11875–11877, 2020.

[64] D. K. Milton, "What was the primary mode of smallpox transmission? implications for biodefense," *Frontiers in cellular and infection microbiology*, vol. 2, p. 150, 2012.

[65] S. B. Leder, D. M. Suiter, and B. G. Green, "Silent aspiration risk is volume-dependent," *Dysphagia*, vol. 26, no. 3, pp. 304–309, 2011.

[66] Speech-Pathology-Australia, "Swallowing Awareness Day." Web link, accessed 16-December-2020.

[67] A. Chakraborty, A. Jorgensen, J. Yuk, C. Chung, L. Chamorro, S. Jung, and S. Basu, "Simulating inhaled transport through bio-inspired pathways in mask filters," *Bulletin of the American Physical Society*, 2020.

[68] J. Yuk, A. Baskota, B. Cooke, K. Frohlich, D. Morton, C. Chung, A. Jorgensen, S. Basu, L. Chamorro, and S. Jung, "3D-printing Mask filters inspired by animal nasal cavity," *Bulletin of the American Physical Society*, 2020.

[69] C. Chung, J. Yuk, A. Jorgensen, S. Basu, S. Jung, and L. Chamorro, "Vortex traps to capture particles with reduced pressure loss in respiratory masks.," *Bulletin of the American Physical Society*, 2020.

[70] J. Yuk, K. Frohlich, R. Connor, S. Basu, L. Chamorro, and S. Jung, "Bio-inspired mask filters with breathing resistance control," *Bulletin of the American Physical Society*, 2021.

[71] M. Kiaee, H. Wachtel, M. L. Noga, A. R. Martin, and W. H. Finlay, "Regional deposition of nasal sprays in adults: A wide ranging computational study," *International Journal for Numerical Methods in Biomedical Engineering*, vol. 34, no. 5, p. e2968, 2018.

[72] K. Zhao, P. W. Scherer, S. A. Hajiloo, and P. Dalton, "Effect of anatomy on human nasal air flow and odorant transport patterns: implications for olfaction," *Chemical Senses*, vol. 29, no. 5, pp. 365–379, 2004.

[73] J. Xi and P. W. Longest, "Numerical predictions of submicrometer aerosol deposition in the nasal cavity using a novel drift flux approach," *International Journal of Heat and Mass Transfer*, vol. 51, no. 23-24, pp. 5562–5577, 2008.

[74] K. T. Shanley, P. Zamankhan, G. Ahmadi, P. K. Hopke, and Y. S. Cheng, "Numerical simulations investigating the regional and overall deposition efficiency of the human nasal cavity," *Inhalation Toxicology*, vol. 20, no. 12, pp. 1093–1100, 2008.

[75] J. T. Kelly, A. K. Prasad, and A. S. Wexler, "Detailed flow patterns in the nasal cavity," *Journal of Applied Physiology*, vol. 89, no. 1, pp. 323–337, 2000.

[76] K. Sato, S. I. Chitose, K. Sato, F. Sato, T. Ono, and H. Umeno, "Sleep-related deglutition and respiratory phase patterns in the aged with obstructive sleep apnea under CPAP therapy," *Acta Oto-Laryngologica*, pp. 1–8, 2020.

[77] K. Shrestha, H. Salati, D. Fletcher, N. Singh, and K. Inthavong, "Effects of head tilt on squeeze-bottle nasal irrigation – A computational fluid dynamics study," *Journal of Biomechanics*, vol. 123, p. 110490, 2021.

[78] L. F. Tracy, S. Basu, P. V. Shah, D. O. Frank-Ito, S. Das, A. M. Zanation, and J. S. Kimbell, "Impact of endoscopic craniofacial resection on simulated nasal airflow and heat transport," in *International Forum of Allergy & Rhinology*, vol. 9, pp. 900–909, Wiley Online Library, 2019.

[79] P. Nithiarasu, "Biofluid Dynamics." Open access link to unpublished textbook, 2021.

[80] P. H. Saksono, P. Nithiarasu, I. Sazonov, and S. Y. Yeo, "Computational flow studies in a subject-specific human upper airway using a one-equation turbulence model. Influence of the nasal cavity," *International Journal for Numerical Methods in Engineering*, vol. 87, no. 1-5, pp. 96–114, 2011.

[81] P. Nithiarasu, O. Hassan, K. Morgan, N. P. Weatherill, C. Fielder, H. Whittet, P. Ebden, and K. R. Lewis, "Steady flow through a realistic human upper airway geometry," *International Journal for Numerical Methods in Fluids*, vol. 57, no. 5, pp. 631–651, 2008.

[82] D. O. Frank-Ito, M. Wofford, J. D. Schroeter, and J. S. Kimbell, "Influence of mesh density on airflow and particle deposition in sinonasal airway modeling," *Journal of aerosol medicine and pulmonary drug delivery*, vol. 29, no. 1, pp. 46–56, 2016.

[83] M. Hall, E. Frank, G. Holmes, B. Pfahringer, P. Reutemann, and I. H. Witten, "The weka data mining software: an update," *ACM SIGKDD explorations newsletter*, vol. 11, no. 1, pp. 10–18, 2009.

[84] I. H. Witten, E. Frank, M. A. Hall, C. J. Pal, and M. DATA, "Practical machine learning tools and techniques," in *Data Mining*, vol. 2, 2005.

[85] H. Moayedi, D. T. Bui, A. Dounis, Z. Lyu, and L. K. Foong, "Predicting heating load in energy-efficient buildings through machine learning techniques," *Applied Sciences*, vol. 9, no. 20, p. 4338, 2019.

[86] J. Brownlee, "How to estimate a baseline performance for your machine learning models in weka," 2016.

[87] X. Su, X. Yan, and C.-L. Tsai, "Linear regression," *Wiley Interdisciplinary Reviews: Computational Statistics*, vol. 4, no. 3, pp. 275–294, 2012.

[88] L. Breiman, "Random forests," *Machine learning*, vol. 45, pp. 5–32, 2001.

[89] T. E. Macrini, "Comparative morphology of the internal nasal skeleton of adult marsupials based on x-ray computed tomography," *Bulletin of the American Museum of Natural History*, vol. 2012, no. 365, pp. 1–91, 2012.

[90] B. A. Craven, E. G. Paterson, G. S. Settles, and M. J. Lawson, "Development and verification of a high-fidelity computational fluid dynamics model of canine nasal airflow," 2009.

[91] C. Casteleyn, A. Broos, P. Simoens, and W. Van Den Broeck, "Nalt (nasal cavity-associated lymphoid tissue) in the rabbit," *Veterinary immunology and immunopathology*, vol. 133, no. 2-4, pp. 212–218, 2010.

[92] M. J. Rodgers, "Cavia porcellus," *Guinea Pig, Digital Morphology. Available at digimorph.*, 2012.

[93] H. Shi, C. Kleinstreuer, and Z. Zhang, "Laminar airflow and nanoparticle or vapor deposition in a human nasal cavity model," 2006.

[94] E. Ghahramani, O. Abouali, H. Emdad, and G. Ahmadi, "Numerical investigation of turbulent airflow and microparticle deposition in a realistic model of human upper airway using LES," *Computers & Fluids*, vol. 157, pp. 43–54, 2017.

[95] J. Lindemann, R. Leiacker, G. Rettinger, and T. Keck, "Nasal mucosal temperature during respiration," *Clinical Otolaryngology & Allied Sciences*, vol. 27, no. 3, pp. 135–139, 2002.

[96] K. Zhao, K. Blacker, Y. Luo, B. Bryant, and J. Jiang, "Perceiving nasal patency through mucosal cooling rather than air temperature or nasal resistance," *PLoS One*, vol. 6, no. 10, p. e24618, 2011.

[97] J. S. Kimbell, D. O. Frank-Ito, P. Laud, G. J. M. Garcia, and J. S. Rhee, "Changes in nasal airflow and heat transfer correlate with symptom improvement after surgery for nasal obstruction," *Journal of Biomechanics*, vol. 46, no. 15, pp. 2634–2643, 2013.

[98] B. A. Craven, T. Neuberger, E. G. Paterson, A. G. Webb, E. M. Josephson, E. E. Morrison, and G. S. Settles, "Reconstruction and morphometric analysis of the nasal airway of the dog (canis familiaris) and implications regarding olfactory airflow," *The Anatomical Record: Advances in Integrative Anatomy and Evolutionary Biology: Advances in Integrative Anatomy and Evolutionary Biology*, vol. 290, no. 11, pp. 1325–1340, 2007.

[99] M. Atramentowicz, "Growth of pouch young in the bare-tailed woolly opossum, caluromys philander," *Journal of mammalogy*, vol. 76, no. 4, pp. 1213–1219, 1995.

[100] I. Wallis, B. Green, and K. Newgrain, "Seasonal field energetics and water fluxes of the long-nosed potoroo (potorous tridactylus) in southern victoria," *Australian Journal of Zoology*, vol. 45, no. 1, pp. 1–11, 1997.

[101] L. M. Jensen, I. R. Wallis, and W. J. Foley, "The relative concentrations of nutrients and toxins dictate feeding by a vertebrate browser, the greater glider petauroides volans," *PLoS One*, vol. 10, no. 5, p. e0121584, 2015.

[102] E. B. Mitchell, M. G. Hawkins, P. M. Gaffney, and A. G. MacLeod, "Gastric dilatation-volvulus in a guinea pig (cavia porcellus)," *Journal of the American Animal Hospital Association*, vol. 46, no. 3, pp. 174–180, 2010.

[103] "Daily pork reports," https://www.ams.usda.gov/market-news/daily-pork-reports.

[104] M. Oakwood, "The ecology of the northern quoll, dasyurus hallucatus," *Ph.D. thesis*, 1997.

[105] C. D. Fryar, M. D. Carroll, Q. Gu, J. Afful, and C. L. Ogden, "Anthropometric reference data for children and adults: United states, 2015-2018," 2021.

[106] A. G. Ford, X. Z. Cao, M. J. Papanikolas, T. Kato, R. C. Boucher, M. R. Markovetz, D. B. Hill, R. Freeman, and M. G. Forest, "Molecular dynamics simulations to explore the structure and rheological properties of normal and hyperconcentrated airway mucus," *Studies in Applied Mathematics*, 2021.

[107] A. Sekaran, "Study of airflow past endotracheal tubes-effect ventilator flow cycles on transport of mucus," in *APS Division of Fluid Dynamics Meeting Abstracts*, pp. H01–007, 2021.

[108] R. R. Rajendran and A. Banerjee, "Effect of non-newtonian dynamics on the clearance of mucus from bifurcating lung airway models," *Journal of Biomechanical Engineering*, vol. 143, no. 2, 2021.

[109] A. V. Kolanjiyil, S. Hosseini, A. Alfaifi, D. Farkas, R. Walenga, A. Babiskin, M. Hindle, L. Golshahi, and P. W. Longest, "Validating CFD predictions of nasal spray deposition:

Inclusion of cloud motion effects for two spray pump designs," *Aerosol Science and Technology*, vol. 56, no. 4, pp. 305–322, 2022.

[110] K. Inthavong, Z. F. Tian, J. Y. Tu, W. Yang, and C. Xue, "Optimising nasal spray parameters for efficient drug delivery using computational fluid dynamics," *Computers in Biology and Medicine*, vol. 38, no. 6, pp. 713–726, 2008.

[111] Y. Feng, J. Zhao, X. Chen, and J. Lin, "An in silico subject-variability study of upper airway morphological influence on the airflow regime in a tracheobronchial tree," *Bioengineering*, vol. 4, no. 4, p. 90, 2017.

[112] J. Zhao, Y. Feng, K. Koshiyama, and H. Wu, "Prediction of airway deformation effect on pulmonary air-particle dynamics: A numerical study," *Physics of Fluids*, vol. 33, no. 10, p. 101906, 2021.

[113] D. Zang, S. Tarafdar, Y. Y. Tarasevich, M. Dutta Choudhury, and T. Dutta, "Evaporation of a Droplet: From physics to applications," *Physics Reports*, vol. 804, pp. 1–56, 2019.

[114] T. A. H. Nguyen, A. V. Nguyen, M. A. Hampton, Z. P. Xu, L. Huang, and V. Rudolph, "Theoretical and experimental analysis of droplet evaporation on solid surfaces," *Chemical engineering science*, vol. 69, no. 1, pp. 522–529, 2012.

[115] S. Chatterjee, J. S. Murallidharan, A. Agrawal, and R. Bhardwaj, "How coronavirus survives for hours in aerosols," *Physics of Fluids*, vol. 33, no. 8, p. 081708, 2021.

[116] S. K. Lai, Y. Y. Wang, D. Wirtz, and J. Hanes, "Micro-and macrorheology of mucus," *Advanced Drug Delivery Reviews*, vol. 61, no. 2, pp. 86–100, 2009.

[117] J. Yuk, A. Chakraborty, S. Cheng, C. I. Chung, A. Jorgensen, S. Basu, L. P. Chamorro, and S. Jung, "On the design of particle filters inspired by animal noses," *Journal of The Royal Society Interface*, vol. 20210849, 2022.

[118] S. D. Delshad, C. V. Almario, W. D. Chey, and B. M. R. Spiegel, "Prevalence of gastroesophageal reflux disease and proton pump inhibitor-refractory symptoms," *Gastroenterology*, vol. 158, no. 5, pp. 1250–1261, 2020.

[119] J. E. Richter and J. H. Rubenstein, "Presentation and epidemiology of gastroesophageal reflux disease," *Gastroenterology*, vol. 154, no. 2, pp. 267–276, 2018.

[120] K. Sato, S. I. Chitose, F. Sato, and H. Umeno, "Deglutition and respiratory patterns during sleep in the aged with OSAS," *Laryngoscope Investigative Otolaryngology*, vol. 3, no. 6, pp. 500–506, 2018.

[121] A. M. Bhutada, W. A. Broughton, and K. L. Focht Garand, "Obstructive sleep apnea syndrome (OSAS) and swallowing function – a systematic review," *Sleep and Breathing*, pp. 1–9, 2020.

[122] J. S. Valbuza, M. M. de Oliveira, E. Zancanella, C. F. Conti, L. B. F. Prado, L. B. C. Carvalho, and G. F. do Prado, "Swallowing dysfunction related to obstructive sleep apnea: a nasal fibroscopy pilot study," *Sleep and Breathing*, vol. 15, no. 2, pp. 209–213, 2011.

[123] K. Sato, S. I. Chitose, K. Sato, F. Sato, T. Ono, and H. Umeno, "Recurrent aspiration pneumonia precipitated by obstructive sleep apnea," *Auris Nasus Larynx*, 2020.

[124] D. McSharry and A. Malhotra, "Potential influences of obstructive sleep apnea and obesity on COVID-19 severity," *Journal of Clinical Sleep Medicine*, vol. 16, no. 9, pp. 1645–1645, 2020.

[125] P. K. Bhatraju, B. J. Ghassemieh, M. Nichols, R. Kim, K. R. Jerome, A. K. Nalla, A. L. Greninger, S. Pipavath, M. M. Wurfel, L. Evans, *et al.*, "COVID-19 in critically ill patients in the Seattle region – case series," *New England Journal of Medicine*, vol. 382, no. 21, pp. 2012–2022, 2020.

[126] M. Arentz, E. Yim, L. Klaff, S. Lokhandwala, F. X. Riedo, M. Chong, and M. Lee, "Characteristics and outcomes of 21 critically ill patients with COVID-19 in Washington State," *JAMA*, vol. 323, no. 16, pp. 1612–1614, 2020.

[127] S. Tufik, D. Gozal, I. A. Ishikura, G. N. Pires, and M. L. Andersen, "Does obstructive sleep apnea lead to increased risk of COVID-19 infection and severity?," *Journal of Clinical Sleep Medicine*, pp. jcsm–8596, 2020.

[128] B. E. Cade, H. S. Dashti, S. M. Hassan, S. Redline, and E. W. Karlson, "Sleep Apnea and COVID-19 mortality and hospitalization," *American Journal of Respiratory and Critical Care Medicine*, vol. 202, no. 10, pp. 1462–1464, 2020.

[129] M. B. Maas, M. Kim, R. G. Malkani, S. M. Abbott, and P. C. Zee, "Obstructive Sleep Apnea and Risk of COVID-19 Infection, Hospitalization and Respiratory Failure," *Sleep and Breathing*, pp. 1–3, 2020.

[130] Cleveland-Clinic, "Can PAP Therapy Machines Increase the Risk of Spreading the Coronavirus?." Web link, accessed 18-December-2020.

[131] S.-E. Amini, V. Gouyer, C. Portal, F. Gottrand, and J.-L. Desseyn, "Muc5b is mainly expressed and sialylated in the nasal olfactory epithelium whereas Muc5ac is exclusively expressed and fucosylated in the nasal respiratory epithelium," *Histochemistry and Cell Biology*, vol. 152, no. 2, pp. 167–174, 2019.

[132] C. F. Kuper, H. Ernst, L. C. van Oostrum, S. Rittinghausen, A. H. Penninks, N.-C. Ganderup, and A. P. Wolterbeek, "Nasal passages of Göttingen minipigs from the neonatal period to young adult," *Toxicologic Pathology*, vol. 40, no. 4, pp. 656–666, 2012.

[133] B. Asgharian, F. J. Miller, O. Price, J. D. Schroeter, D. R. Einstein, R. A. Corley, and T. Bentley, "Modeling particle deposition in the pig respiratory tract," *Journal of Aerosol Science*, vol. 99, pp. 107–124, 2016.

[134] M. Zhi, X. Zhang, K. Zhang, S. J. Ussher, W. Lv, J. Li, J. Gao, Y. Luo, and F. Meng, "The characteristics of atmospheric particles and metal elements during winter in Beijing: Size distribution, source analysis, and environmental risk assessment," *Ecotoxicology and Environmental Safety*, vol. 211, p. 111937, 2021.

[135] F. Kermen, A. Chakirian, C. Sezille, P. Joussain, G. Le Goff, A. Ziessel, M. Chastrette, N. Mandairon, A. Didier, C. Rouby, *et al.*, "Molecular complexity determines the number of olfactory notes and the pleasantness of smells," *Scientific Reports*, vol. 1, p. 206, 2011.